Engineering Analysis with Boundary Elements 134 (2022) 259–281

Contents lists available at ScienceDirect

Engineering Analysis with Boundary Elements

journal homepage: www.elsevier.com/locate/enganabound

A NURBS-discontinuous and enriched isogeometric boundary element formulation for two-dimensional fatigue crack growth

H.C. Andrade [a,*], J. Trevelyan [b,*], E.D. Leonel [a,*]

[a] Department of Structural Engineering, São Carlos School of Engineering, University of São Paulo. Av. Trabalhador São Carlense, 400, 13566-590. São Carlos-SP, Brazil

[b] Department of Engineering, Durham University, South Road, Durham DH1 3LE, UK

ARTICLE INFO

Keywords:
Extended isogeometric boundary element method
Isogeometric analysis
NURBS
Enriched formulations
Linear elastic fracture mechanics
Fatigue crack growth

ABSTRACT

A new extended isogeometric boundary element method (XIGABEM) formulation is proposed for simulating multiple fatigue crack propagation in two-dimensional domains. The classical use of NURBS in isogeometric formulations is further extended by repeated knot insertion to introduce a C^{-1} continuity within the approximation space as an elegant approach to representing geometrical discontinuities at crack intersections. This strategy is also used to restrict the enrichment term to the portion of the NURBS defining the tip, where it is necessary. At this near-tip zone, the linear elastic fracture mechanics solutions are embedded into the displacement approximation to represent the theoretical square root behaviour. The enrichment procedure introduces just two degrees of freedom per crack tip, and a tying constraint is used to yield a square linear system. In this *direct* approach, the stress intensity factors (SIFs) are found as terms in the solution vector without requiring post-processing techniques.

Several examples are presented to illustrate the application of the XIGABEM. The accuracy of the results compares favourably against those from the literature, and also against solutions obtained from unenriched and enriched indirect methods that employ the J-integral for SIF extraction. Furthermore, the proposed direct approach is capable of significantly reducing the execution time.

1. Introduction

Since the seminal paper of Hughes et al. [1], the isogeometric analysis (IGA) concepts have been extensively embedded in different numerical methods for applications in several fields. In IGA, the same functions employed by computer-aided design (CAD) packages are used for both accurate geometry description and approximation of the unknown quantities. One of the advantages of this approach over the conventional polynomial-based formulations is the remarkable reduction of effort for the mesh generation process since the discretisation is provided directly by the CAD model. This is particularly beneficial for industrial applications, in which the mesh generation can take up to 80% of overall analysis time [1,2]. Moreover, the basis functions adopted by IGA facilitate the refinement process using knot insertion or degree elevation without changing the geometry or its parametrisation.

Engineering components are commonly expressed in CAD systems in the form of surface models or boundary representations. Therefore, the coupling between IGA and domain-based methods, such as the finite element method (FEM) [2–9], requires the definition of an additional parametrisation direction to define the domain discretisation, which can be a quite complex task [10]. Alternatively, boundary-based numerical techniques, such as the boundary element method (BEM), provide a more natural and direct link between CAD models and numerical analysis since both formulations deal with quantities solely on the boundary. Early application of IGA into the BEM was made by Politis et al. [11], in which an exterior planar Neumann problem was analysed. Later, Simpson et al. [12,13] introduced the fundamentals and implementation aspects of IGA for elastostatic BEM. In these works, the term IGABEM was coined for the numerical approach. The use of the IGABEM has since expanded, and the method has been applied to several problems involving geomechanics [14,15], acoustics [16–18], shape optimisation [19–21], potential flow [22,23], heat transfer [24] and fracture [25–28]. Additionally, studies concerning the accurate evaluation of the singular and near-singular integrals arising in IGABEM can be found in [29–31].

When dealing with linear-elastic crack problems, the IGA basis functions are not themselves capable of accurately representing the mechanical behaviour in the singular zone near the crack tips. This drawback can be overcome with an enrichment strategy, in which

* Corresponding authors.
E-mail addresses: heider.andrade@usp.br (H.C. Andrade), jon.trevelyan@durham.ac.uk (J. Trevelyan), edleonel@sc.usp.br (E.D. Leonel).

https://doi.org/10.1016/j.enganabound.2021.09.019
Received 9 June 2021; Received in revised form 24 August 2021; Accepted 22 September 2021
Available online 23 October 2021

the displacement approximation is augmented with functions based on the analytical near-tip solution [32–34]. The development of numerical methods combining the benefits of extended and isogeometric analysis (XIGA) has received much attention, especially in the FEM framework [35–39]. Meanwhile, the use of XIGA in the BEM context – resulting in the XIGABEM, also denoted as XIBEM in the literature – is still incipient. The first applications of XIGABEM were reported by Peake et al. [40,41], in which 2D and 3D Helmholtz problems were analysed. Regarding crack problems, Peng et al. [42] adopted a crack tip enrichment based on the partition of unity (PU) similar to the approach used by Simpson and Trevelyan [43] in an extended BEM (XBEM) formulation. Some shortcomings of PU-based enrichment are the number of additional degrees of freedom and the ill-conditioning of the resulting system of equations. Also, new collocation points are required to retrieve a square system of equations, and the optimal location of these points is not clear.

Noting that the additional degrees of freedom in the PU-based enrichment for XBEM are all proxies for the SIFs, an alternative was proposed by Simpson and Trevelyan [44], in which the displacement approximation was augmented in a similar fashion to the early work of Benzley [45]. In this strategy, the number of additional degrees of freedom introduced by the enrichment is limited to two per tip for planar problems. Including a crack tip tying constraint in this approach, Alatawi and Trevelyan [46] were able to accommodate the additional degrees of freedom without additional collocation points, and also showed how the SIFs could be obtained directly from the system of equations with sufficient accuracy. This later feature is particularly beneficial in boundary element formulations, since indirect approaches for computing the SIFs, such as the J-integral [47], are computationally costly due to the need for evaluating internal fields. Notwithstanding this additional cost, the enrichment strategy can also be combined with post-processing techniques to markedly improve the accuracy of computed SIF values for cases in which highly accurate solutions are required [46,48].

In this paper, we develop an XIGABEM formulation for the direct evaluation of SIFs. A propagation scheme considering the enriched approach is also proposed for the analysis of fatigue crack growth in two-dimensional bodies. As is usual in IGA formulations, non-uniform rational B-splines (NURBS) basis functions are applied. The higher-order continuity provided by NURBS facilitates the definition of collocation points on the crack with the required continuity for the existence of the finite part integrals presented in the dual boundary element formulation [49,50] adopted here. For crack propagation analysis, the new crack surfaces are created from the extension of existing NURBS. A C^{-1} continuity for the rational basis is enforced between the new and old surfaces to limit the enrichment term to the portion near the crack tip, where it is necessary. The availability of C^{-1} continuity is also elegantly exploited to represent the geometrical discontinuity in elements intersected by cracks simply by inserting the required knots. Therefore, the description of the NURBS is maintained and the use of more elaborate strategies for introducing the discontinuity, such as an enrichment based on the Heaviside function, can be dismissed. Two sets of examples are presented to demonstrate the accuracy of the proposed XIGABEM formulation. The first set is concerned with the evaluation of SIFs, whereas the second deals with fatigue crack propagation problems, including the prediction of fatigue life. The results are compared with analytical, experimental and numerical solutions available in the literature. Besides, the direct XIGABEM approach is contrasted with unenriched and enriched indirect methods that employ the J-integral for SIF extraction.

The novel aspects of the present work are as follows:

- the direct evaluation of stress intensity factors in the solution vector in an IGABEM formulation, which extends the state of art in this framework. The XIGABEM approach allows the computation of accurate solutions, including for curved cracks, with reduced computational effort and using coarse meshes. These accurate results are found without the further expense of post-processing techniques such as a J-integral. Additionally, if we choose to incur the extra cost of such post-processing, results of very high accuracy can be recovered.
- the modelling of fatigue crack growth using an XIGABEM formulation. The proposed enriched approach introduces small modifications to the unenriched formulation and BEM matrices, which facilitates its implementation in existing IGABEM codes.
- the introduction of a C^{-1}-continuous (i.e. discontinuous) NURBS basis to facilitate isogeometric modelling of discontinuities such as the intersection of cracks with other boundaries. This strategy allows the representation of geometrical gaps simply by the application of a standard knot insertion algorithm to the existing NURBS definition. The C^{-1} continuity is also applied to facilitate the crack extension and the definition of the enriched portion of NURBS describing the crack tips.

The remainder of this paper is structured as follows: Section 2 briefly describes the NURBS basis functions. The inclusion of C^{-1} continuity in the NURBS basis through knot insertion is also discussed. Section 3 presents the novel XIGABEM formulation used to improve the response near crack tips and to define the SIFs directly from the system of equations. Section 4 shows how XIGABEM is applied for simulating fatigue crack growth. Several examples are presented in Section 5. Finally, Section 6 draws some conclusions about the extended isogeometric approach developed in this study.

2. NURBS

2.1. NURBS definitions

NURBS have been extensively applied in CAD software for geometry modelling. Among their advantages are the exact representation of conic sections and quadric surfaces and the ability to describe complex forms, such as industrial components. In the present investigation, NURBS basis functions are adopted in the isogeometric formulation, and a brief description is given in what follows. Further details about NURBS can be obtained in Piegl and Tiller [51] and Hughes et al. [1].

Firstly, we define the B-spline basis functions, which are used to construct the NURBS. Given a knot vector $\Xi = \{\xi_1, \xi_2, \ldots, \xi_{n+p+1}\}$, the B-spline functions of order p are evaluated by the Cox–de Boor recursion formula [52,53]:

$$N_{i,0}(\xi) = \begin{cases} 1, & \xi_i \le \xi < \xi_{i+1} \\ 0, & otherwise, \end{cases} \tag{1}$$

for $p = 0$ (constant B-spline) and:

$$N_{i,p}(\xi) = \frac{\xi - \xi_i}{\xi_{i+p} - \xi_i} N_{i,p-1}(\xi) + \frac{\xi_{i+p+1} - \xi}{\xi_{i+p+1} - \xi_{i+1}} N_{i+1,p-1}(\xi) \tag{2}$$

for $p \ge 1$. $N_{i,p}$ indicates the ith B-spline function, with $i = 1, \ldots, n$, while n represents the number of basis functions defined over the parametric space $\xi \in [\xi_1, \xi_{n+p+1}]$. In the applications of this paper we assume that the initial and final knots are repeated $p+1$ times at the start and end of Ξ. In this case, the knot vector is termed as open knot vector.

Using Eqs. (1) and (2) and considering a set of positive weights $Y = \{w_1, w_2, \ldots, w_n\}$, in which each value w_i is associated with $N_{i,p}$, the NURBS basis functions become:

$$R_{i,p}(\xi) = \frac{N_{i,p}(\xi) w_i}{\sum_{j=1}^{n} N_{j,p}(\xi) w_j} \tag{3}$$

The NURBS basis functions defined in Eq. (3) are non-negative and form a partition of unity, i.e., $\sum_{i=1}^{n} R_{i,p}(\xi) = 1$, $\forall \xi$. Moreover, it can be noted that they degenerate into the B-spline functions if all weights are equal.

The NURBS derivatives can also be computed recursively by the expressions given in Appendix A. In general, NURBS functions are C^{p-1}

continuous over $[\xi_1, \xi_{n+p+1}]$. However, if a knot value appears q times in the knot vector (i.e. has multiplicity equal to q), the continuity of the NURBS at that knot becomes C^{p-q}.

After defining the NURBS basis functions, a 2-D NURBS curve can be obtained by the linear combination of products of $R_{i,p}$ and the positions of a set of n control points as:

$$\tilde{x}_j(\xi) = \sum_{i=1}^{n} R_{i,p}(\xi) x_j^i \tag{4}$$

where $\tilde{x}_j(\xi)$ ($j = 1, 2$ for 2-D) denotes the coordinates of the NURBS curve at ξ and $\mathbf{p}^i = (x_1^i, x_2^i)$ are the coordinates of the ith control point.

To illustrate the NURBS concepts, Fig. 1(a) shows the distribution of the rational basis functions obtained with the knot vector and weights presented in the figure and considering $p = 2$. It can be observed that the functions are C^0 continuous in knots with multiplicity $q = p$. Fig. 1(b) shows how the rational functions from Fig. 1(a) can be associated with the control points to describe a unit circle exactly.

2.2. Knot insertion and continuity of NURBS basis

When adopting the isogeometric approach in a numerical method, the refinement of NURBS is often required to increase the mesh density for the analysis. In this paper, the refinement process is performed with the knot insertion strategy, which is analogous to h-refinement of conventional isoparametric elements. There are some other alternatives for NURBS refinement, such as order elevation or k-refinement [1], but they are not considered in the present investigation.

In the knot insertion strategy, knots are introduced into the knot vector and the control point locations and weights modified to preserve the exact geometry of the resulting spline. Given an open knot vector $\Xi = \{\xi_1, \xi_2, \ldots, \xi_{n+p+1}\}$, let $\bar{\xi} \in [\xi_a, \xi_{a+1}[$ be a desired new knot. The new $n+1$ rational basis functions are constructed in the standard way by applying Eq. (3) considering the new knot vector $\bar{\Xi} = \{\xi_1, \xi_2, \ldots, \xi_a, \bar{\xi}, \xi_{a+1}, \ldots \xi_{n+p+1}\}$. To define the new control points positions and weights for the 2-D NURBS, we firstly define the coordinate $\mathbf{Q}^i = (x_1^i w^i, x_2^i w^i, w^i) \in \mathbb{R}^3$ considering the position $\mathbf{p}^i = (x_1^i, x_2^i)$ and weight w^i of the ith original control point. Then, the modified coordinates $\bar{\mathbf{Q}}^i$ are computed as follows [51]:

$$\bar{\mathbf{Q}}^i = \alpha^i \mathbf{Q}^i + (1 - \alpha^i)\, \mathbf{Q}^{i-1} \tag{5}$$

where:

$$\alpha^i = \begin{cases} 1, & 1 \le i \le a-p \\ \frac{\bar{\xi} - \xi_i}{\xi_{i+p} - \xi_i}, & a-p+1 \le i \le a \\ 0, & a+1 \le i \le n+p+2 \end{cases} \tag{6}$$

After application of Eq. (5), the modified coordinates $\bar{\mathbf{Q}}^i = (\bar{x}_1^i \bar{w}^i, \bar{x}_2^i \bar{w}^i, \bar{w}^i)$ are obtained. This new set of points in $\mathbb{R}^3$ can be projected back to $\mathbb{R}^2$ to recover the new set of control points and weights for the given NURBS after the knot insertion. Hence, the new control points positions are given by $\bar{\mathbf{p}}^i = (\bar{x}_1^i, \bar{x}_2^i)$, with corresponding weight equals to $\bar{w}^i$.

Successive knot insertions can also be applied to introduce discontinuities into a NURBS when necessary. This is achieved by performing multiple knot insertions until a knot value reaches multiplicity $q = p+1$. In other words, if a particular knot $\bar{\xi}$ has multiplicity $p+1$, the rational basis becomes C^{-1} continuous (i.e. discontinuous) at $\bar{\xi}$. In this study, the C^{-1} continuity is used to facilitate the remeshing process during crack propagation. Details about this strategy are given in Section 4.2.

Considering the illustrative example shown in Fig. 1(a), the NURBS basis functions presented in Fig. 2(a) are obtained after three successive knot insertions at $\bar{\xi} = 1.5$. Note that the knot insertions modify the rational functions defined over the knot span $[1.0, 2.0[$, which contains the considered $\bar{\xi}$. Three new basis functions are created – each one introduced by a knot insertion – while the former three rational functions defined over the interval are altered. Essentially, the knot spans on the left and right of $\bar{\xi} = 1.5$ behave as two independent NURBS due to the C^{-1} continuity that has been introduced. Fig. 2(b) presents the new control point positions generated after the knot insertions for the unit circle geometry. At the end of the process, control points 5 and 6 are coincident. Since the NURBS basis functions are discontinuous at this point, a geometric discontinuity may be represented if the coincident control points are moved to different locations.

3. Extended isogeometric boundary element method

3.1. Boundary integral equations for elastostatic

The applications in this paper are based on 2-D linear elastostatic formulation. Let Ω denote an isotropic and elastic domain with enclosing boundary Γ, as illustrated in Fig. 3. The linear elastostatic boundary value problem may expressed in terms of boundary integral equations by considering a point-load problem in an infinite domain. Details about the derivation can be found in Aliabadi [54].

When analysing bodies containing cracks, as illustrated in Fig. 3, the application of the same boundary integral equation at coincident source points $\mathbf{x}'$ and $\bar{\mathbf{x}}'$ on the opposing crack surfaces leads to degeneracy in the resulting system of algebraic equations. One approach to overcome this deficiency is the use of two independent boundary integral equations: the Displacement Boundary Integral Equation (DBIE) and the Traction Boundary Integral Equation (TBIE) [49,50]. The DBIE is applied to $\mathbf{x}'$ on the upper crack surface Γ^+, and its expression – neglecting body forces – is given by:

$$c_{ij}(\mathbf{x}')u_j(\mathbf{x}') + c_{ij}(\bar{\mathbf{x}}')u_j(\bar{\mathbf{x}}') + \fint_\Gamma P_{ij}^*(\mathbf{x}', \mathbf{x})u_j(\mathbf{x})\, d\Gamma = \int_\Gamma U_{ij}^*(\mathbf{x}', \mathbf{x})p_j(\mathbf{x})\, d\Gamma \tag{7}$$

in which u_j and p_j represent the displacement and traction components, respectively; U_{ij}^* and P_{ij}^* are the displacement and traction fundamental solutions, respectively, and B presents their expressions for 2-D problems; $\fint$ denotes an integral to be evaluated in the Cauchy principal value sense; $c_{ij}u_j$ represents the jump arising from the integration of the strongly singular kernel P_{ij}^*. The explicit expressions to compute c_{ij} can be found in Guiggiani and Casalini [55] and, for $\mathbf{x}'$ at smooth boundaries, $c_{ij} = \delta_{ij}/2$, where δ_{ij} is the Kronecker delta. It is worth mentioning that Eq. (7) is also applied to source points $\mathbf{x}'$ placed at the non-crack boundaries. In this case, the jump term $c_{ij}(\bar{\mathbf{x}}')u_j(\bar{\mathbf{x}}')$ vanishes since there is no coincident point $\bar{\mathbf{x}}'$.

The TBIE can be obtained after differentiation of the DBIE (7) with respect to $\mathbf{x}'$ and further substitution into generalised Hooke's law. This process increases the order of the singularity of the integral kernels presented in the integral equation. For the existence of the resulting finite part integrals, the TBIE must be applied to locations at which the displacement derivatives are continuous. This constrains us to place $\mathbf{x}'$ at a smooth boundary and to ensure that the basis functions at that point exhibit the required continuity. Then, considering $\mathbf{x}'$ to be located on a smooth portion of the lower crack surfaces Γ^-, the TBIE is written as:

$$\frac{1}{2}\left[p_j(\mathbf{x}') - p_j(\bar{\mathbf{x}}')\right] + n_i(\mathbf{x}') \fint_\Gamma S_{kij}^*(\mathbf{x}', \mathbf{x})u_k(\mathbf{x})\, d\Gamma = n_i(\mathbf{x}') \int_\Gamma D_{kij}^*(\mathbf{x}', \mathbf{x})p_k(\mathbf{x})\, d\Gamma \tag{8}$$

where $\fint$ stands for the Hadamard principal value integral; $n_i(\mathbf{x}')$ are the components of the outward unit normal vector at the source point; D_{kij}^* and S_{kij}^* are obtained from the derivatives of U_{ij}^* and P_{ij}^*, respectively. The expressions for D_{kij}^* and S_{kij}^* are also given in Appendix B.

3.2. Numerical implementation of XIGABEM

3.2.1. Approximations

For an accurate numerical integration of the DBIE (7) and TBIE (8), the NURBS describing the geometry may be subdivided into boundary elements, following a concept similar to the conventional isoparametric

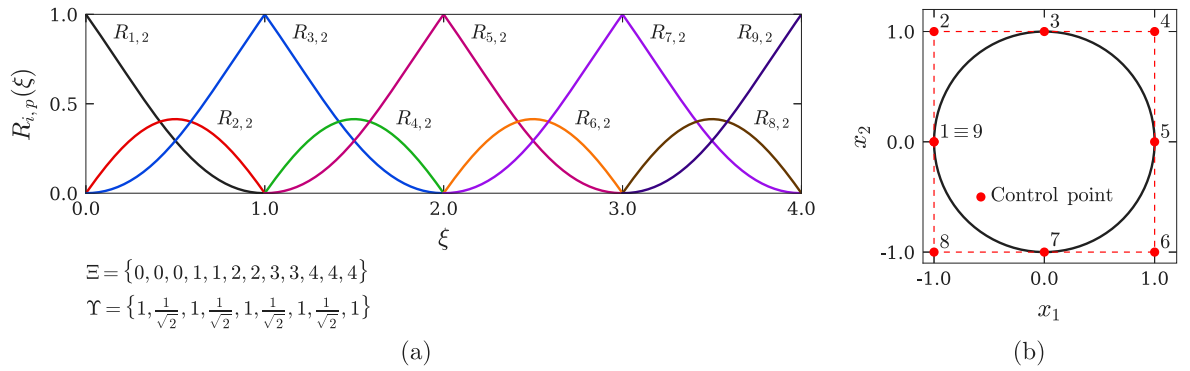

Fig. 1. Representation of (a) the NURBS basis functions and (b) the NURBS curve representing a unit circle. The order of the NURBS is $p = 2$.

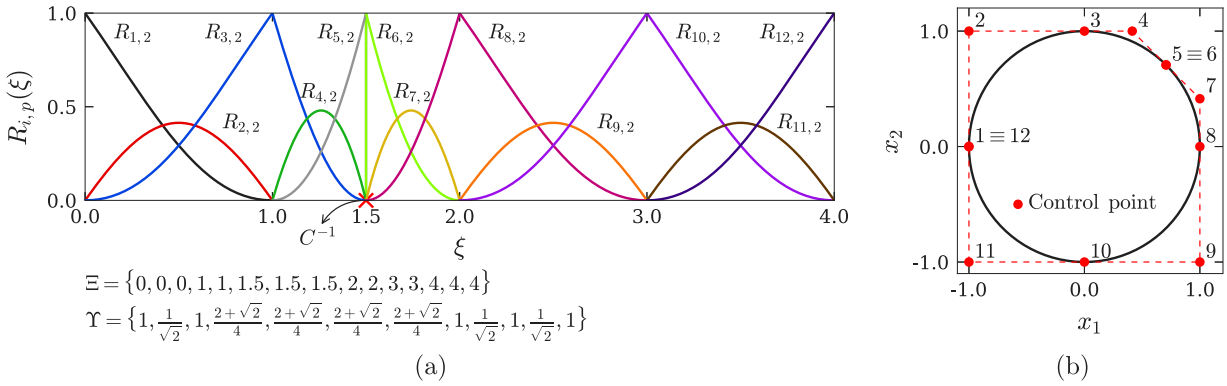

Fig. 2. (a) NURBS basis functions after $p+1$ knot insertions at $\bar{\xi} = 1.5$. (b) Representation of the NURBS curve and new control points positions. Control points 5 and 6 end up in the same position after the successive knot insertions; however, the NURBS curve may be discontinuous at this point if the coincident control points are moved to different locations.

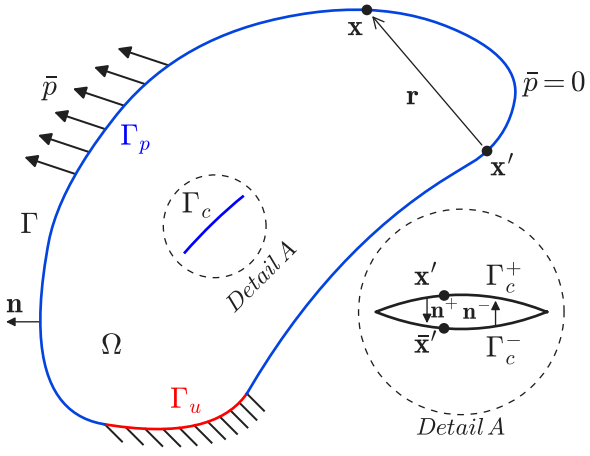

Fig. 3. Representation of a cracked body.

BEM. For the isogeometric analysis, a boundary element is defined in the parametric space as the span between two distinct knots of a NURBS, or formally $\xi \in [\xi_a, \xi_{a+1}[\ : \ \xi_a \neq \xi_{a+1}$. From the recursive nature of the rational basis functions presented in Section 2.1, the only non-zero functions over an element are $R_{a-p,p}, R_{a-p+1,p}, \ldots, R_{a,p}$ (see Figs. 1(a) and 2(a) for graphical examples). It is interesting to note that the number of non-zero basis functions is equal to $p+1$, as observed when adopting Lagrangian elements in BEM, and the control points to which they are associated define the connectivity of the isogeometric element. Hence, the coordinates over an element e can be evaluated from:

$$\tilde{x}_j^e(\xi) = \sum_{m=1}^{p+1} \phi^{em}(\xi) x_j^{em} \qquad \xi \in [\xi_a, \xi_{a+1}[\ : \ \xi_a \neq \xi_{a+1} \tag{9}$$

where the terms $\phi^{em}(\xi) = R_{i,p}(\xi)$ represent the mth shape function of order p from element e, with $i = m + a - p - 1$. Additionally, x_j^{em} denotes the coordinates of the mth local control point of the element.

Fig. 4 highlights an element along a NURBS curve defined from the parametric space. However, it is suitable to define the boundary elements over the parent space $\hat{\xi} \in [-1, 1]$ (see Fig. 4) in order to apply the Gauss–Legendre quadrature for numerical integration. The linear transformation that maps the parameter ξ to $\hat{\xi}$ is given by:

$$\xi = \frac{(\xi_{a+1} - \xi_a)\,\hat{\xi} + (\xi_{a+1} + \xi_a)}{2} \tag{10}$$

and the Jacobian of the transformation from the parent space $\hat{\xi}$ to the Cartesian coordinate system is evaluated by the chain rule as:

$$J^e(\hat{\xi}) = \frac{d\Gamma^e}{d\xi} \frac{d\xi}{d\hat{\xi}} \tag{11}$$

with $\frac{d\Gamma^e}{d\xi}(\xi) = \sqrt{\left(\frac{d\tilde{x}_1^e}{d\xi}(\xi)\right)^2 + \left(\frac{d\tilde{x}_2^e}{d\xi}(\xi)\right)^2}$ and $\frac{d\xi}{d\hat{\xi}} = \frac{(\xi_{a+1} - \xi_a)}{2}$.

When considering the isogeometric approach, the unknown boundary fields along the elements are also approximated through the same rational bases used for representing the geometry involved. However, the NURBS basis functions, as the Lagrange polynomials in conventional BEM, fail to accurately represent the square root behaviour near crack tips predicted by the LEFM theory. To capture the analytical behaviour and, consequently, improve the near-tip numerical solution, an extended formulation may be employed. In this paper, we adopt the displacement approximation enrichment introduced by Simpson and Trevelyan [44] within the XBEM framework, which was based on the

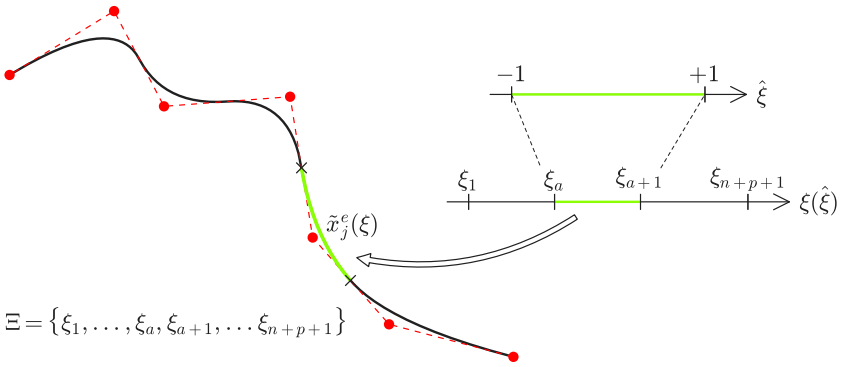

Fig. 4. Mapping between the Cartesian, parametric and the parent spaces.

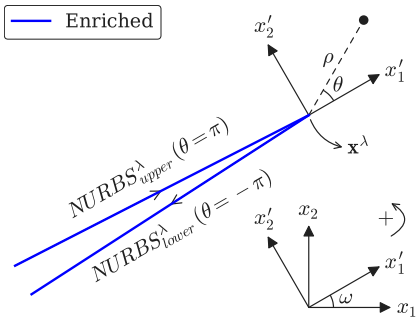

Fig. 5. Local coordinate system at an enriched crack tip.

early work of Benzley [45]. Extending this strategy to an XIGABEM approach, the displacement approximation for an element e over a crack surface defining a tip λ is written as:

$$\tilde{u}_j^{e\lambda}(\xi) = \sum_{m=1}^{p+1} \phi^{em}(\xi) d_j^{em} + \sum_{M=I,II} \tilde{K}_M^\lambda T_{jk}^\lambda \psi_{kM}(\mathbf{x}^\lambda, \mathbf{x}(\xi)) \tag{12}$$

The first term on the right-hand side of Eq. (12) is the standard IGABEM expansion of the displacement into products of the NURBS basis functions ϕ^{em} and the displacement control variables d_i^{em} associated with the mth local control point. This term is responsible for capturing any non-zero displacement at the crack tip. It should be noted that, since the NURBS basis functions are usually not interpolatory, i.e. do not exhibit the Kronecker delta property at the control points (see, for example, the NURBS curve in Fig. 4), the displacement control variables do not directly represent displacements on the boundary of the body. The second term of the right-hand side of Eq. (12) exactly represents the leading-order term from Williams expansion for displacements [56] (see Eq. (D.1)), and it is introduced in the approximation to capture the near-tip behaviour. This term contains the additional parameters $\tilde{K}_M^\lambda = \tilde{K}_I^\lambda, \tilde{K}_{II}^\lambda$ included by the enrichment, and these become unknowns that, when found as part of the BEM solution vector, provide the stress intensity factors. We note that they become accurate approximations only if we enforce continuity of displacement at the crack tip (see Section 3.2.2), which is the exact same condition observed in the analytical solution. The crack tip functions ψ_{kM} are extracted directly from the asymptotic solution given by Williams [56], and they are expressed in matrix notation as:

$$\begin{bmatrix} \psi_{1I} & \psi_{1II} \\ \psi_{2I} & \psi_{2II} \end{bmatrix} = \frac{1}{2\mu}\sqrt{\frac{\rho}{2\pi}} \begin{bmatrix} \cos\left(\frac{\theta}{2}\right)(\kappa - \cos\theta) & \sin\left(\frac{\theta}{2}\right)(\kappa + 2 + \cos\theta) \\ \sin\left(\frac{\theta}{2}\right)(\kappa - \cos\theta) & -\cos\left(\frac{\theta}{2}\right)(\kappa - 2 + \cos\theta) \end{bmatrix} \tag{13}$$

where ρ is the distance to the tip and θ is the angular variation according to the local coordinate system positioned at the crack tip $\mathbf{x}^\lambda$, as shown in Fig. 5. κ represents the Kolosov constant defined as $\kappa = 3 - 4\nu$ for plane strain and $\kappa = (3 - \nu)/(1 + \nu)$ for plane stress.

To transform the contribution of the enrichment functions from the local to the global coordinate system, the components T_{jk}^λ of the rotation matrix are also included in the enrichment term of Eq. (12), in which:

$$\begin{bmatrix} T_{11}^\lambda & T_{12}^\lambda \\ T_{21}^\lambda & T_{22}^\lambda \end{bmatrix} = \begin{bmatrix} \cos\omega & -\sin\omega \\ \sin\omega & \cos\omega \end{bmatrix} \tag{14}$$

where ω is the angle between the local and global coordinates systems (see Fig. 5).

The displacement approximation expressed in Eq. (12) is used only for boundary elements on NURBS defining the crack tips. Then, the square root behaviour observed in the near-tip solution can be captured through the enrichment term. For the other elements, only the rational basis contribution is considered in the displacement approximation.

Although the stress components in the leading-order term of Williams expansion present the well-known $\mathcal{O}(1/\sqrt{\rho})$ singularity, the tractions obtained from these components are zero over the crack surfaces. This result is expected since the analytical solution contemplates traction-free cracks. Therefore, the approximation used for elements at cracks, as well as for elements along the external boundary, is expressed solely through the NURBS basis functions as:

$$\tilde{p}_j^e(\xi) = \sum_{m=1}^{p+1} \phi^{em}(\xi) t_j^{em} \tag{15}$$

where t_j^{em} denotes the traction parameters associated with the mth local control point from element e.

Eqs. (9), (12) and (15) can be substituted into Eqs. (7) and (8) to define the discrete forms of the boundary integral equations. Special attention should be given to the jump terms, since both u_j and p_j at the source point $\mathbf{x}'$ (or at the coincident point $\bar{\mathbf{x}}'$, if it exists) must be written considering, respectively, the displacement and traction approximations for the element e' containing $\mathbf{x}'$ (or element $\bar{e}'$ containing $\bar{\mathbf{x}}'$). Hence, the discrete form of the DBIE can be written as follows:

$$\sum_{m=1}^{p+1} c_{ij}(\mathbf{x}'(\xi'))\phi^{e'm}(\xi') d_j^{e'm} + \sum_{m=1}^{p+1} c_{ij}(\bar{\mathbf{x}}'(\bar{\xi}'))\phi^{\bar{e}'m}(\bar{\xi}') d_j^{\bar{e}'m} + \\ + \sum_{e=1}^{N_e}\sum_{m=1}^{p+1} P_{ij}^{em} d_j^{em} + \sum_{\lambda=1}^{N_t}\sum_{M=I,II}\tilde{K}_M^\lambda \sum_{e=1}^{N_e^\lambda} \tilde{P}_{iM}^{e\lambda} = \sum_{e=1}^{N_e}\sum_{m=1}^{p+1} U_{ij}^{em} t_j^{em} \tag{16}$$

where N_e is the total number of elements, N_t is the number of enriched crack tips and N_e^λ is the number of elements enriched in the vicinity of the tip λ. It is worth mentioning that the enrichment functions do not modify the jump term in the DBIE (12) since the crack tip functions ψ_{kM} for coincident source points $\mathbf{x}'$ and $\bar{\mathbf{x}}'$ cancel each other out during implementation. The boundary integrals P_{ij}^{em} and U_{ij}^{em}, written in terms of the parent space $\hat{\xi}$, are given by:

$$P_{ij}^{em} = \int_{-1}^{1} P_{ij}^*(\mathbf{x}', \mathbf{x}(\hat{\xi}))\phi^{em}(\hat{\xi}) J^e(\hat{\xi}) d\hat{\xi} \tag{17}$$

$$U_{ij}^{em} = \int_{-1}^{1} U_{ij}^{*}(\mathbf{x}', \mathbf{x}(\hat{\xi}))\phi^{em}(\hat{\xi})J^{e}(\hat{\xi})d\hat{\xi} \tag{18}$$

and the boundary integral containing the enrichment functions is computed from:

$$\tilde{P}_{iM}^{e\lambda} = \int_{-1}^{1} P_{ij}^{*}(\mathbf{x}', \mathbf{x}(\hat{\xi}))T_{jk}^{\lambda}\psi_{kM}(\mathbf{x}^{\lambda}, \mathbf{x}(\hat{\xi}))J^{e}(\hat{\xi})d\hat{\xi} \tag{19}$$

Analogously, the discrete TBIE is determined as:

$$n_i(\mathbf{x}'(\xi'))\left(\sum_{e=1}^{N_e}\sum_{m=1}^{p+1} S_{kij}^{em}d_k^{em} + \sum_{\lambda=1}^{N_t}\sum_{M=I,II}\tilde{K}_M^{\lambda}\sum_{m=1}^{N_e^{\lambda}}\tilde{S}_{ijM}^{e\lambda}\right) = \tag{20}$$
$$= -\frac{1}{2}\left[\sum_{m=1}^{p+1}\phi^{e'm}(\xi')t_j^{e'm} - \sum_{m=1}^{p+1}\phi^{\bar{e}'m}(\bar{\xi}')t_j^{\bar{e}'m}\right] + n_i(\mathbf{x}'(\xi'))\sum_{e=1}^{N_e}\sum_{m=1}^{p+1}D_{kij}^{em}t_k^{em}$$

where:

$$S_{kij}^{em} = \neq\int_{-1}^{1} S_{kij}^{*}(\mathbf{x}', \mathbf{x}(\hat{\xi}))\phi^{em}(\hat{\xi})J^{e}(\hat{\xi})d\hat{\xi} \tag{21}$$

$$D_{kij}^{em} = \int_{-1}^{1} D_{kij}^{*}(\mathbf{x}', \mathbf{x}(\hat{\xi}))\phi^{em}(\hat{\xi})J^{e}(\hat{\xi})d\hat{\xi} \tag{22}$$

$$\tilde{S}_{ijM}^{e\lambda} = \neq\int_{-1}^{1} S_{kij}^{*}(\mathbf{x}', \mathbf{x}(\hat{\xi}))T_{kp}^{\lambda}\psi_{pM}(\mathbf{x}^{\lambda}, \mathbf{x}(\hat{\xi}))J^{e}(\hat{\xi})d\hat{\xi} \tag{23}$$

The use of the enriched displacement approximation in Eq. (12) only introduces the terms related to the enrichment parameters $\tilde{K}_I^{\lambda}$ and $\tilde{K}_I^{\lambda}$ in Eqs. (16) and (20), while the other terms are exactly the same as they would be in an unenriched formulation. Therefore, the number of degrees of freedom introduced by the enrichment is limited to two per crack tip, regardless of the number of enriched elements, which is an advantage of the applied strategy over PU-based enrichments [42,43]. This reduced number of enrichment parameters is also beneficial for the conditioning of the system of equations. The next section presents the additional relations adopted in the proposed XIGABEM formulation that accommodate the additional enrichment parameters and allow the direct evaluation of the SIFs.

3.2.2. Crack tip tying constraint

To accommodate the degrees of freedom introduced by the enrichment and, consequently, recover a square system of equations, the crack tip tying constraint proposed by Alatawi and Trevelyan [46] is extended to the XIGABEM framework. This condition aims to enforce the continuity of the displacements between the upper and lower crack surfaces at the tip, which is not guaranteed in the unenriched approach as independent NURBS are used to model each crack surface (see Fig. 5). When compared to XBEM, the definition of the constraint is simplified by the use of NURBS functions to replace the conventional Lagrangian basis.

Using the displacement approximation shown in Eq. (12), and since open knot vectors are used in the definition of the basis functions, the displacement at the crack tip considering the NURBS at the upper surface ($\theta = \pi$) is $\tilde{u}_j^{U}(\xi_{n+p+1}) = d_j^{U_{tip}}$, where $d_j^{U_{tip}}$ is the displacement parameter of the control point positioned at the end of the upper NURBS. Similarly, the displacement at the crack tip considering the NURBS at the lower surface ($\theta = -\pi$) is $\tilde{u}_j^{L}(\xi_1) = d_j^{L_{tip}}$, where $d_j^{L_{tip}}$ is the displacement parameter of the control point positioned at the start of the lower NURBS. Thus, the displacement continuity condition at the tip is simply expressed as:

$$d_j^{U_{tip}} - d_j^{L_{tip}} = 0 \tag{24}$$

Eq. (24) provides two supplementary equations per crack tip and this is exactly sufficient to yield a square system of equations. Since the continuity condition at the tip is the same as observed in the Williams expansion, the additional parameters $\tilde{K}_I^{\lambda}$ and $\tilde{K}_{II}^{\lambda}$ represent a good approximation for mode I (K_I^{λ}) and mode II (K_{II}^{λ}) SIFs. Therefore, the proposed XIGABEM strategy allows the SIFs to be computed directly from the system of equations, eliminating the need for computationally expensive post-processing techniques, such as the widely applied J-integral.

3.2.3. Assembly of the system of equations

With the discrete forms of the DBIE (16) and the TBIE (20), the algebraic system of equations obtained by the XIGABEM is assembled by applying the collocation method. The positions of the collocation points in the parametric space are defined through the Greville abscissae [57,58] defined as:

$$\xi_i' = \frac{\sum_{j=1}^{p}\xi_{i+j}}{p} \tag{25}$$

in which ξ_i' is the knot corresponding to the ith collocation point along the NURBS. The Cartesian coordinates of this point can be determined by Eq. (9).

For the analysis of crack problems, the DBIE (16) is used for the collocation points at the external boundary and at one of the crack surfaces, whereas the TBIE (20) is applied for the collocation points at the other surface to obtain a non-singular system of equations. During the collocation process, the collocation points become the source point $\mathbf{x}'(\xi')$ of their respective boundary integral equations.

The existence of the Hadamard principal value in the TBIE requires the continuity of the displacement derivatives at the collocation points. Thus, the continuity feature of the NURBS facilitates the positioning of the collocation points over the crack surfaces. Adopting NURBS basis functions with $p > 2$ is sufficient to ensure the smoothness of the displacements along the entire surface, except at points in which the continuity is reduced by repeated knots. At these particular points, as the initial and final points of the NURBS, the collocation points must be shifted inside the curve. To satisfy the continuity condition in these cases, the corresponding Greville abscissa must be modified. For example, when considering the first and last collocation points on the NURBS, their coordinates in the parametric space are updated to $\xi_1' = \xi_1' + \chi\left(\xi_2' - \xi_1'\right)$ and $\xi_n' = \xi_n' - \chi\left(\xi_n' - \xi_{n-1}'\right)$, respectively, where χ is a shifting parameter. In this paper, we assume $\chi = 0.2$. We note that different values for χ may affect the numerical solutions near the crack tips, particularly when considering IGABEM. In XIGABEM, as the enrichment term is responsible for representing the square root behaviour near the tip, the choice of χ is found not to have a significant effect on the results.

Due to the singularities of the fundamental solutions when the field point $\mathbf{x}(\xi)$ approaches the source point $\mathbf{x}'(\xi')$ (see expressions in Appendix B), the integral kernels in Eqs. (17), (18), (19), (21), (22) and (23) must be evaluated with different strategies depending on the position of the source point in relation to the integrated element. When the source point is far from the element, the integrands are regular and standard Gauss–Legendre quadrature is applied for numerical evaluation. For source points close to the integrated element, the integrands become quasi-singular. In this case, Telles' third-degree polynomial transformation [59,60] is used to improve the accuracy of the integration. To evaluate the integral kernels for an element that contains the source point, the integrand must be firstly regularised. For the weakly singular kernel U_{ij}^{em} given in Eq. (18), Telles' third-degree polynomial transformation is applied for regularisation. However, a special integration scheme should be considered for the strongly singular and hypersingular integrals. In these situations, the singularity subtraction method (SSM) may be used, and Appendix C.1 presents the expression implemented in this study to compute the conventional and enriched singular kernels.

After the collocation process is carried out for each collocation point in the mesh, and including the crack tip tying constraint given by Eq. (24), the resulting algebraic system of equations defined by XIGABEM is assembled as:

$$\begin{bmatrix} \mathbf{H} & \mathbf{H}_C^{\lambda} \\ \mathbf{H}_R^{\lambda} & \mathbf{0} \end{bmatrix}\begin{Bmatrix} \mathbf{d} \\ \tilde{\mathbf{K}} \end{Bmatrix} = \begin{bmatrix} \mathbf{G} \\ \mathbf{0} \end{bmatrix}\{\mathbf{t}\} \tag{26}$$

in which $\mathbf{H}$ is determined from the boundary integrals P_{ij}^{em} and S_{kij}^{em} and from the distribution of the jump terms in the DBIE. $\mathbf{G}$ is obtained from the boundary integrals U_{ij}^{em} and D_{kij}^{em} and from the distribution of the jump terms in the TBIE. $\mathbf{d}$ and $\mathbf{t}$ are vectors containing, respectively, the displacement and traction control parameters, while $\tilde{\mathbf{K}}$ is a vector storing the additional unknowns, $\tilde{K}_I^{\lambda}$ and $\tilde{K}_{II}^{\lambda}$ for each crack tip λ, introduced by the enrichment. The sub-matrix related to the enriched parameters $\mathbf{H}_C^{\lambda}$ is composed of the enriched integrals $\tilde{P}_{iM}^{e\lambda}$ and $\tilde{S}_{ijM}^{e\lambda}$, whereas $\mathbf{H}_R^{\lambda}$ is defined from the crack tip tying constraints. It is important to point out that the crack tip enrichment given by Eq. (12) only introduces the sub-matrices $\mathbf{H}_C^{\lambda}$ and $\mathbf{H}_R^{\lambda}$ into the system of equations. The other components of the system ($\mathbf{H}$, $\mathbf{G}$, $\mathbf{d}$ and $\mathbf{t}$) are the same as they would be in an unenriched IGABEM formulation.

Imposing the prescribed boundary conditions to the system in Eq. (26), the final system of linear equations is determined as follows:

$$\begin{bmatrix} \mathbf{A} & \mathbf{H}_C^{\lambda} \\ \mathbf{H}_R^{\lambda} & \mathbf{0} \end{bmatrix} \begin{Bmatrix} \mathbf{x} \\ \tilde{\mathbf{K}} \end{Bmatrix} = \begin{Bmatrix} \mathbf{f} \\ \mathbf{0} \end{Bmatrix} \tag{27}$$

where $\mathbf{A}$ is a $2N \times 2N$ matrix composed of the coefficients from $\mathbf{H}$ and $\mathbf{G}$ related to the unknown control variables, with N being the total number of collocation points in the model. $\mathbf{x}$ is a $2N$ vector containing the unknown control parameters and $\mathbf{f}$ is a $2N$ vector obtained from the multiplication of the known control values and their respective influence coefficients from matrices $\mathbf{H}$ and $\mathbf{G}$. For completeness, the dimensions of the other terms are given as follows: $\mathbf{H}_R^{\lambda}$ and $\mathbf{H}_C^{\lambda}$ are, respectively, a $2N_t \times 2N$ and a $2N \times 2N_t$ matrix, while $\tilde{\mathbf{K}}$ is a $2N_t$ vector.

The solution of the linear system of equations defined by XIGABEM, Eq. (27), yields values for the unknown control parameters and also for the SIFs without the need of a post-processing scheme since they appear in the solution vector, represented by the term $\tilde{\mathbf{K}}$. The mechanical fields at any point $\mathbf{x}(\xi)$ on the boundary, including the collocation points, can be recovered element-wise from Eqs. (12) (or its unenriched counterpart) and (15) considering the approximation for the element e containing ξ.

4. XIGABEM for fatigue crack growth

For the XIGABEM analyses described in this paper, the structural boundary is imported directly from CAD software. The cracks are then inserted in the model, with each surface defining one crack tip given by a NURBS, as illustrated in Fig. 6(a). The knot vector for the NURBS at the upper surface is defined over $\xi^U \in [0, 1]$, whereas at the lower surface it is described over $\xi^L \in [-1, 0]$. Therefore, the parameters ξ for corresponding points at each crack surface satisfy $\xi^U = -\xi^L$. As also illustrated in Fig. 6(a), the whole NURBS containing a crack tip in the initial configuration is enriched with the tip functions.

Then, the NURBS are refined by splitting the knot vector in uniform knot spans corresponding to the boundary elements. Furthermore, if a crack is defined such that it intersects a geometric boundary, a knot refinement at the intersection point is performed until a C^{-1} continuity is reached for the crossed NURBS. Therefore, this scheme utilises the intrinsic properties of NURBS and is an elegant way to represent the discontinuity at the crack mouth.

After defining the boundary element mesh, the linear system of equations can be assembled following the formulation described in Section 3. The solution of the system given by XIGABEM leads to direct evaluation of the SIFs for the crack tips. The XIGABEM can also be employed in conjunction with post-processing techniques, such as the ones based on the J-integral, to improve the accuracy of the indirect method, as will be discussed in the examples in Section 5.

4.1. Fatigue analysis

In the applications of this paper, we consider oscillatory loadings in the structure that induce fatigue crack growth. High-cycle fatigue is assumed, in which the stress levels introduced by the oscillatory loading are well below the material's yield strength and the strains observed within the structure are predominantly elastic. To define the crack growth rate in these applications, we adopt the Paris law [61]:

$$\frac{da}{dN} = C\left(\Delta K_{ef}\right)^m \tag{28}$$

where da/dN represents the crack extension per load cycle, in which a is the crack length and N is the number of load cycles, C and m are material constants. The range of effective stress intensity factors for mixed-mode can be computed, according to Tanaka [62], as $\Delta K_{ef} = \sqrt[4]{\Delta K_I^4 + 8\Delta K_{II}^4}$, in which $\Delta K_M = K_M^{max} - K_M^{min}$, with K_M^{max} and K_M^{min} representing, respectively, the maximum and minimum values of the considered SIF within a load cycle. For simplicity, we assume that the crack propagation follows the power law in Eq. (28) throughout the analyses. Alternatively, another growth law could also be coupled to the XIGABEM formulation developed herein.

For applications involving multiple cracks, each crack tip grows proportionally to its growth rate following the relationship:

$$\Delta a = \Delta L \frac{C\left(\Delta K_{ef}\right)^m}{\left[da/dN\right]^{\lambda_d}} \tag{29}$$

where Δa is the crack length increment, ΔL is the standard crack length increment defined in the analysis and $\left[da/dN\right]^{\lambda_d}$ is the highest crack growth rate observed during one load cycle and related to the dominant tip λ_d.

It is worth emphasising that in mechanical problems involving multiple cracks, some of them may grow faster than others. Different crack growth rates may lead to very small crack length increments and, consequently, collocation points may be positioned very close to their neighbours. This situation introduces numerical instabilities into the final system of algebraic equations given by the boundary integral formulation because of the singular nature of the fundamental solutions. To avoid such issue, the virtual crack extension scheme proposed by Price and Trevelyan [63] is adopted in the numerical approach. In this strategy, the crack tip only propagates if the crack length increment is higher than a prescribed ratio of ΔL, assumed here as $0.1\Delta L$. If this condition is not satisfied, then Δa is accumulated as a virtual length. During the course of the analysis, if the total virtual extension satisfies the growth condition, the crack is extended by the accumulated length.

The number of load cycles ΔN_{i+1} to extend a crack by $\Delta a = a_{i+1} - a_i$ can be computed by integration of the Paris law (28). Assuming a linear variation of ΔK_{ef} between a_i and a_{i+1}, the following discrete expression is defined [64]:

$$\Delta N_{i+1} = \frac{\Delta a}{C\,(m-1)} \frac{\left[\left(\Delta K_i\right)^{1-m} - \left(\Delta K_{i+1}\right)^{1-m}\right]}{\left(\Delta K_{i+1} - \Delta K_i\right)} \tag{30}$$

where ΔK_i and ΔK_{i+1} are the values of ΔK_{ef} at the crack lengths a_i and a_{i+1}, respectively.

4.2. Propagation and remeshing

To define the direction of the discrete length increment given by Eq. (29), we adopt the predictor–corrector scheme proposed by Portela et al. [65]. This strategy aims to take into account the variation of the SIFs during the stable fatigue crack growth to obtain the same crack path independently of the selected crack length increment. The prediction of the propagation angle at each iteration of the algorithm is computed with the maximum circumferential stress criterion [66] as follows:

$$\theta_p = \sin^{-1}\left(\frac{K_I K_{II} - 3K_{II}\sqrt{8K_{II}^2 + K_I^2}}{9K_{II}^2 + K_I^2}\right) \tag{31}$$

The steps of the predictor–corrector scheme are listed below:

(1) For the current crack configuration η, compute the propagation direction $\theta^i_{p(\eta)}$ for the first iteration considering Eq. (31).
(2) Extend the crack tip by Δa, computed from Eq. (29), along the direction determined in the previous step.
(3) Compute the SIFs for the new crack configuration $\eta+1$.
(4) Evaluate a new propagation direction $\theta^i_{p(\eta+1)}$ from Eq. (31) considering the new SIFs obtained from step 3.
(5) Define the correction angle $\beta^i = \theta^i_{p(\eta+1)}/2$.
(6) Correct the crack tip increment defined in the second step to the new growth direction given by $\theta^{i+1}_{p(\eta)} = \theta^i_{p(\eta)} + \beta^i$.
(7) Return to step 2 while $|\beta^i| < \left|\beta^{i-1}\right|$ and $\left|\beta^i/\theta^i_{p(\eta)}\right| > \delta$, where $\delta = 10^{-3}$ in the present study.

After evaluating the propagation direction, the NURBS defining the growing tip are extended to the new tip position, as shown by Fig. 6(b). This is achieved by expanding the corresponding knot vectors by a unit and defining new control points that represent the geometry of new crack surfaces. In the example given in Fig. 6(b), after the propagation of tip $\lambda = 1$, the NURBS at the upper and lower surfaces become defined over $\xi^U \in [0,2]$ and $\xi^L \in [-2,0]$, respectively. Additionally, the multiplicity of the knot corresponding to the former tip is kept equal to $p+1$, so that a C^{-1} continuity occurs between the new and old crack surfaces. This discontinuity is adopted in the present work to make the approximations over the newly created crack surfaces completely independent from the quantities in the existing surfaces. As illustrated in Fig. 6(b), the enrichment is applied only to the elements over the new crack surfaces, where the dominant square root behaviour is captured by the enriched displacement approximation given in Eq. (12). For the elements defining the old crack surfaces, the unenriched approximation is adopted, which is able to represent the displacement fields since there is no singular behaviour along this region.

The changes in the geometry during the crack propagation are accompanied by modifications to the system of equations given by Eq. (27). After a crack increment, as illustrated in Fig. 6(b), most of the system remains unaltered since a C^{-1} continuity is enforced between the old and new crack surfaces. As represented by the graphical representation of the algebraic system in Fig. 7(a), only the enrichment sub-matrices related to the growing tip need to be reconstructed in this case, whereas the other terms are expanded to include the degrees of freedom associated with the new crack surfaces.

If a crack tip intersects a boundary during propagation, as shown by Fig. 6(c), successive knot insertions are considered for the crossed NURBS until a C^{-1} continuity is obtained at the intersection point so that a displacement discontinuity may be represented. The additional columns and rows associated with the enrichment parameters of the intersecting tip are removed from the system of equations as the tip becomes inactive and no longer benefits from enrichment (Fig. 7(b)). Moreover, the positions related to the modified control and collocation points in intersected NURBS are also reconstructed in the original system.

As a final remark before moving on to study some numerical applications, we comment that the implementation of knot insertion to achieve C^{-1} continuity along the growing crack and at crack intersections appears a particularly elegant use of the properties of NURBS and is restricted to IGABEM. This simple expedient removes the need for the definition of discontinuous and semi-discontinuous elements in Lagrangian formulations, and therefore saves a considerable amount of careful data management and the use of different sets of shape functions.

5. Numerical applications

Two sets of examples are presented to illustrate the application of the proposed direct XIGABEM formulation to simulate crack problems. In the first group, we analyse the effect of the enrichment in the accuracy and the convergence rate of the SIF values. In the second set of problems, we use the numerical approach for fatigue crack propagation modelling. The results obtained by the enriched method are compared with those determined using unenriched IGABEM and other solutions available in the literature. Additionally, the run times determined by the enriched and unenriched approaches are compared in some of the examples to demonstrate the benefit of the proposed direct method.

For the numerical analyses, the order of these NURBS functions is selected as 2. Moreover, we assume a 30-point Gaussian quadrature rule for the evaluation of the integral kernels, the same amount used by Peng et al. [42]. The use of this high order scheme is motivated by a desire to present errors as those resulting from the formulation and its discretisation, i.e. with negligible pollution of the results from integration errors. All numerical simulations are performed on a personal computer with Intel® Core™ i7-8750H @ 2.20 GHz processor and 16 GB of RAM.

We emphasise that in our proposed direct approach the stress intensity factors are found directly in the solution vector (see terms $\tilde{\mathbf{K}}^\lambda_I$ and $\tilde{\mathbf{K}}^\lambda_{II}$ at the bottom of the solution vector in Fig. 7(a), for example). We show how these direct evaluations of the SIFs are of appropriate engineering accuracy without the requirement for further post-processing, e.g. a J-integral, which can save a significant amount of computational time as will be demonstrated by several applications that follow. However, we also investigate the further enhancement of the accuracy of our predictions of the SIFs that can be realised by including such a post-processing stage, and it is for this purpose that we also compute the SIFs indirectly using the interaction integral strategy [67] based on the J-integral [47]. When considering the unenriched formulation, the SIFs are also computed using this scheme. For this post-processing strategy, the integration path is considered circular, centred at the crack tip and starting at the third collocation point counting from the tip. Consistent with the isogeometric philosophy, the integration path is defined as a NURBS discretised into sixteen elements.

5.1. Evaluation of SIFs

5.1.1. Square plate with an edge crack

In this first example, we analyse the square plate containing an edge crack shown in Fig. 8. Pure mode loadings are considered by prescribing the analytical displacements given by Eq. (D.1) as Dirichlet boundary conditions along the edges of the plate, while the crack surfaces are treated as traction-free. For the analyses, we assume $a = 1$, $L = 2$, $E = 1$, $\nu = 0.3$ and a plane strain state. The numerical solutions are compared with the exact solutions and also with the results provided by Peng et al. [42], in which the IGABEM and an XIGABEM formulation based on PU-enrichment were applied.

Initially, we assess the accuracy and convergence rate of the proposed XIGABEM formulation with respect to the displacements in a pure mode I problem ($K_I = 1$ and $K_{II} = 0$). A fixed number of eight elements is used in the discretisation of each edge of the plate, while the number of elements along the crack surfaces is varied. Fig. 9 shows the deformed shape for the upper crack surface determined by the unenriched and enriched formulations considering five elements along the crack. It can be noted that the result obtained by IGABEM differs from the analytical solution particularly near the crack tip since the NURBS basis functions are not capable of capturing the square root behaviour in this region. On the other hand, the enriched approximation can approximate the exact response with remarkable precision. Fig. 10 shows the convergence of the errors in the relative L^2 displacement error norm e_{L2}, which we define as:

$$e_{L2} = \frac{\|u^{num} - u^{ana}\|_{L^2(\Gamma_c)}}{\|u^{ana}\|_{L^2(\Gamma_c)}} \tag{32}$$

in which u^{num} and u^{ana} are the displacement solutions given numerically and analytically, respectively, and Γ_c denotes the crack surfaces. The

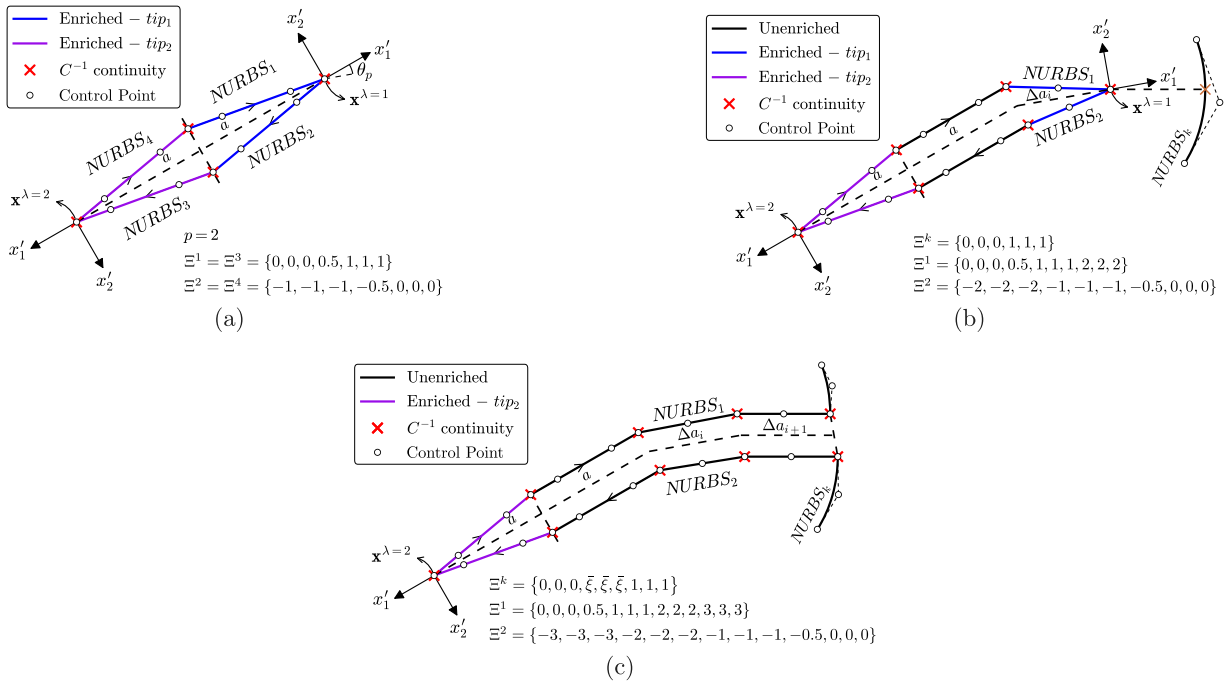

Fig. 6. (a) Representation of enriched NURBS for an interior crack. In this example, the basis functions are assumed with order $p=2$ and each NURBS is initially discretised into two elements (two knot spans in the knot vector). (b) NURBS and their enriched parts after a crack tip propagation. Each new NURBS segment is discretised into one element (one additional knot span in the knot vector) and the multiplicity for the knot at the former tip is kept equals to $p+1$. (c) Intersection between the crack tip $\lambda=1$ with another NURBS, which is initially discretised into one element in the illustrative example. In this case, the respective crack NURBS no longer benefit from enrichment. Besides, the crossed NURBS is made discontinuous at the intersection by increasing the multiplicity of the intersection knot $\bar{\xi}$ to $p+1$ through successive knot insertions. After this processed, the intersected NURBS becomes discretised into two elements, each defined by independent control points.

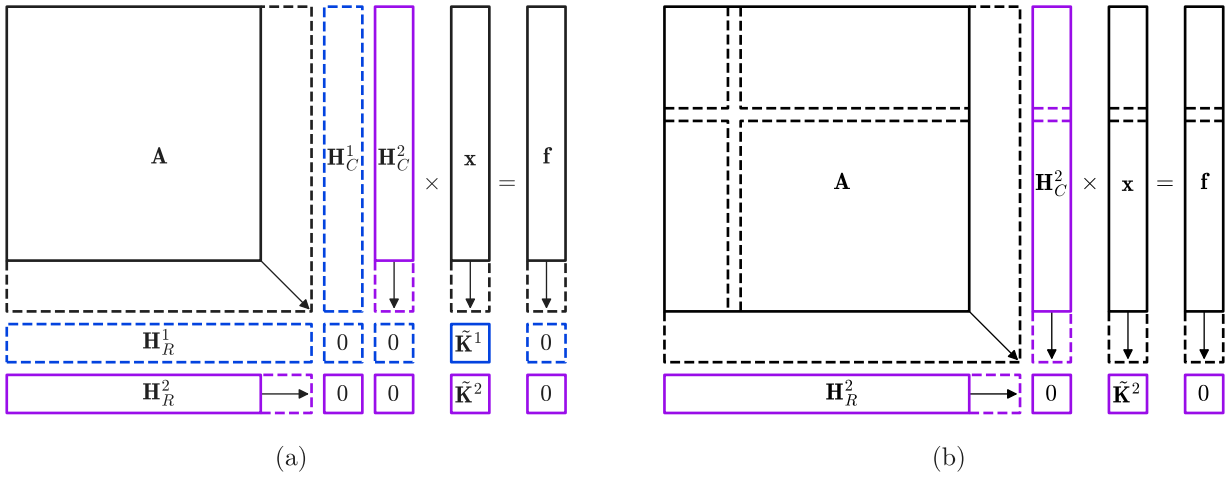

Fig. 7. Graphical representation of the changes in the sub-matrices from the system of equations resulting from (a) the crack propagation illustrated in Fig. 6(b) and (b) the crack propagation followed by the intersection of a NURBS depicted in Fig. 6(c). Note that most of the sub-matrices remain unaltered (represented by solid lines). The changes in the system (represented by dashed lines) are related to the enrichment parameters related to the growing tip and the new control/collocation points defined along the new crack surfaces and intersected NURBS.

L^2 norm of a vector quantity $\mathbf{g}=(g_x,g_y)^T$ is evaluated using $\|\mathbf{g}\|_{L^2(\Gamma_c)}=\sqrt{\int_{\Gamma_c}\mathbf{g}^T\mathbf{g}d\Gamma}$.

The results in Fig. 10 show that the accuracy and convergence rate obtained by the unenriched IGABEM model are similar to those determined by Peng et al. [42]. Regarding the enriched formulations, the PU-enrichment approach used by Peng et al. [42] is capable of improving the convergence rate to 1.53 for a sufficiently fine mesh. This strategy includes the square root behaviour of the displacements near the tip, which improves the accuracy when compared to the unenriched approach, but continuity at the crack tip is not guaranteed. In the proposed XIGABEM formulation, the crack tip function embedded into the displacement approximation can markedly improve the accuracy of the results, giving errors around 2.0×10^{-5} even for coarse crack meshes. The errors in this case depend fundamentally on how well the analytical displacement can be represented by the basis functions along the external boundary. This can be observed by the curve presented in Fig. 10 for an enriched model considering just four elements along each edge of the plate, in which the errors are increased to approximately 2.0×10^{-4}.

The reason for the errors in displacements to be practically constant in the XIGABEM model is that the displacements along the crack surfaces are fundamentally given by the enrichment term in the displacement approximation (see Eq. (12)), whereas the contribution from

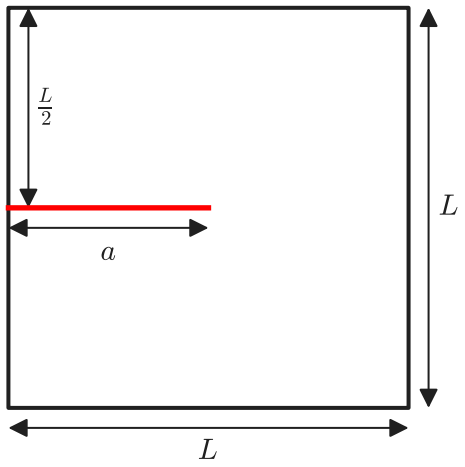

Fig. 8. Square plate with an edge crack.

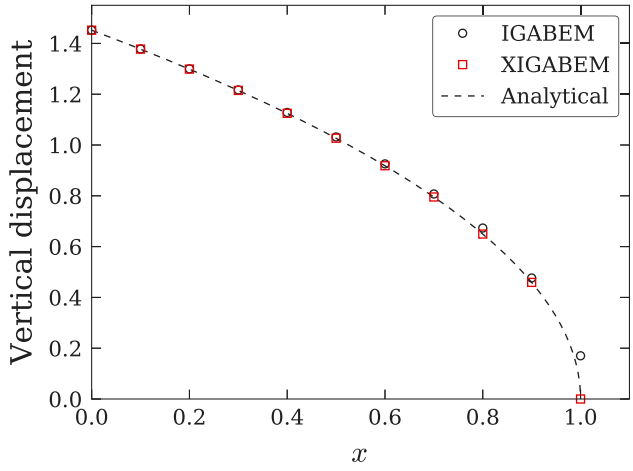

Fig. 9. Deformed shape for the upper crack surface determined by IGABEM and XIGABEM.

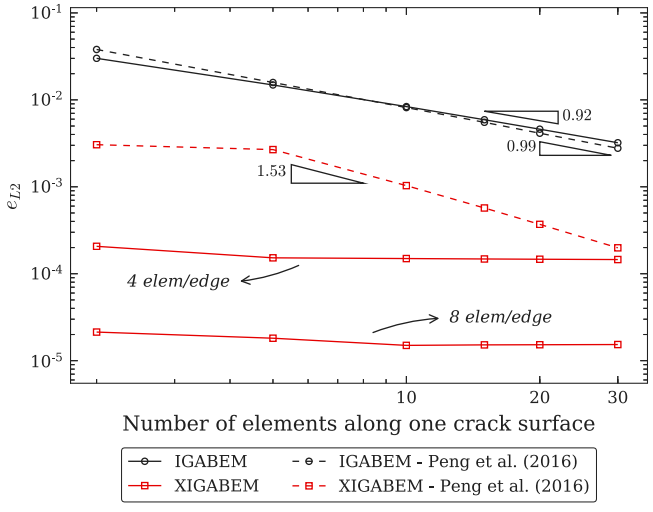

Fig. 10. Relative L^2 displacement error norm e_{L2} (Eq. (32)) along the crack surfaces. The reference results are taken from Peng et al. [42].

the NURBS basis functions is negligible. Consequently, the crack mesh refinement has little effect on the error convergence. The contribution of each term in the displacements is illustrated in the sequence depicted in Fig. 11. Figs. 11(a) and 11(b) present the deformed shape considering the contribution from the NURBS basis functions and the enrichment term, respectively, while the superposition of both responses gives the deformed shape in Fig. 11(c). From the sequence, it can be noted that the displacements along the crack are indeed controlled by the enrichment term, while the deformed shape of the external boundary is exclusively given by the basis functions since the corresponding NURBS are not enriched.

Considering now a mixed-mode problem in which $K_I = 1$ and $K_{II} = 1$, we analyse the accuracy of the SIF values determined by the numerical models. The SIFs are computed directly from the system of equations by the proposed XIGABEM formulation and also indirectly with the J-integral approach. Fig. 12 shows the convergence for K_I and K_{II} with the number of DOF in the numerical model. As in the displacement analysis, the accuracy and convergence rate for IGABEM are similar to the solutions obtained by Peng et al. [42]. Moreover, the direct approach is capable of giving very accurate solutions, with errors in the order of 0.011% for both SIFs even for coarse meshes. Furthermore, the combination of the enriched formulation and the J-integral approach can significantly improve the accuracy, giving errors as low as 0.0004%, but at the expense of computing internal points fields. Again, the mesh refinement has little effect in the convergence of the SIFs values since the near-tip behaviour is mainly controlled by the enrichment term.

It is, of course, expected that for these pure mode problems the enriched formulation should give excellent results because the solution is contained in the approximation space. We now move on to explore examples in which this is not the case.

5.1.2. *Finite rectangular plate with an edge crack under bending*

The rectangular plate containing an edge crack shown in Fig. 13 is considered in this second example. The structure is submitted to pure bending applied through linearly varying distributed loads ranging from -$\bar{\sigma}$ to $\bar{\sigma}$, as depicted in Fig. 13. The dimensions of the plate and the crack are related by $h = 2.5w$ and $a = 0.5w$, and we take the values $\bar{\sigma} = 1$, $w = 2$, $E = 1$ and $\upsilon = 0$ to perform the analyses. Alatawi and Trevelyan [46] also simulated this problem considering an XBEM formulation similar to the one adopted here, but instead of the NURBS basis functions, they applied the conventional Lagrange polynomials in the displacement approximation. The reference solution provided by Fett [68] is used to assess the accuracy of the numerical models.

Fig. 14(a) presents the evolution of K_I (normalised by $\bar{\sigma}\sqrt{\pi a}$) with mesh refinement. It can be noted that the solutions obtained by the present study and by Alatawi and Trevelyan [46] tend to converge towards the reference value given by Fett [68], plotted as a horizontal dashed line. Fig. 14(b) shows the convergence pattern in each scenario. Concerning the unenriched formulations, the IGABEM is able to increase both the accuracy and the convergence rate when compared to conventional BEM. Besides, the enriched formulations increase the accuracy and convergence rate over their unenriched counterparts. Regarding the direct method for SIF extraction, XIGABEM solutions are more accurate than those determined using XBEM. However, the convergence rates obtained by these formulations are similar. For both XBEM and XIGABEM, the lowest errors and highest convergence rate are given by associating the enriched formulation with the J-integral technique. When the XIGABEM is considered in this case, the error in K_I is around 0.25% for the coarsest mesh used, reducing to 0.0016% with mesh refinement.

The contribution of each term in the displacement approximation to the deformed shape of the structure is illustrated in Fig. 15. Unlike the previous example, there is now a non-zero contribution from the NURBS basis functions to the crack response since the enrichment functions are unable to describe the behaviour over the entire crack. However, the near tip behaviour continues to be strongly influenced by the enrichment term.

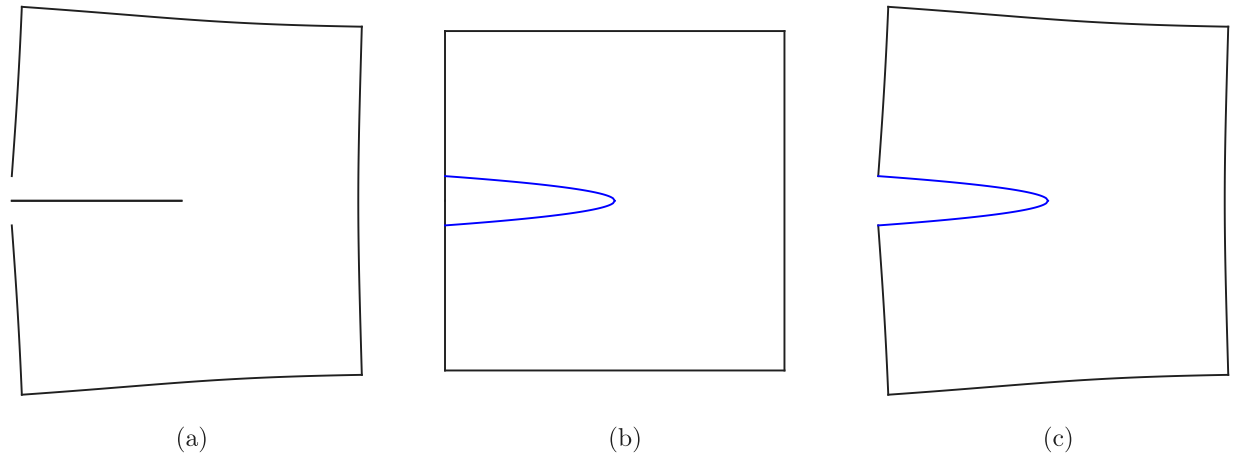

Fig. 11. Deformed shapes considering the contribution from (a) the NURBS basis functions and (b) the enrichment term. (c) Final deformed shape for pure mode I problem, given by the superposition of solutions from (a) and (b). The enriched NURBS are depicted in blue (please refer to the coloured version).

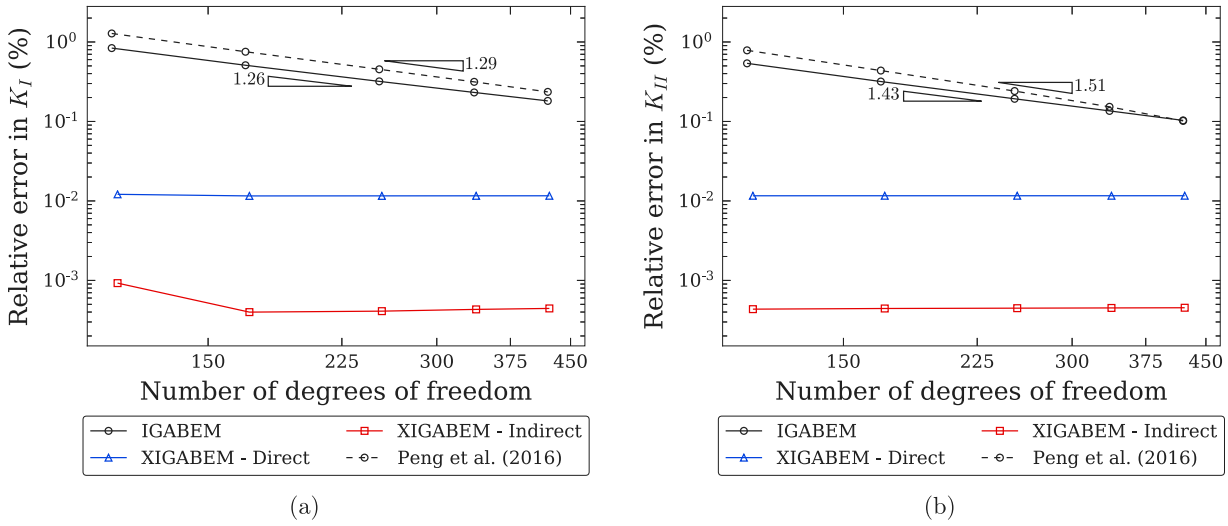

Fig. 12. Convergence of (a) mode I and (b) mode II SIF.

5.1.3. Crack in an infinite domain

In this example, we analyse two cases of cracks immersed in an infinite domain and subjected to a far-field vertical loading $\bar{p}$. Case (a) presents the problem of an inclined crack, whereas Case (b) shows the analysis of a circular arc crack. The infinite domain formulation presented in Brebbia et al. [69] is applied, so only the crack surfaces are discretised. For all analyses, we assume $2a = 1$, $\bar{p} = 1$, $E = 1$, $\upsilon = 0.3$ and plane strain condition. The results for the SIFs are compared with the analytical solutions that can be found in Tada et al. [70]:

$$\left\{ \begin{array}{c} K_I \\ K_{II} \end{array} \right\} = \bar{p}\sqrt{\pi a}\cos\theta \left\{ \begin{array}{c} \cos\theta \\ \sin\theta \end{array} \right\} \tag{33}$$

for the inclined crack problem and:

$$\left\{ \begin{array}{c} K_I \\ K_{II} \end{array} \right\} = \frac{\bar{p}\sqrt{\pi a}}{2\left[1+\sin^2\left(\frac{\theta}{2}\right)\right]} \times \left\{ \begin{array}{c} \cos\left(\frac{\theta}{2}\right)\left[2-4\sin^2\left(\frac{\theta}{2}\right)-3\sin^4\left(\frac{\theta}{2}\right)\right] \\ \sin\left(\frac{\theta}{2}\right)\left[4-2\sin^2\left(\frac{\theta}{2}\right)-3\sin^4\left(\frac{\theta}{2}\right)\right] \end{array} \right\} \tag{34}$$

for the circular arc crack problem.

Case (a): Inclined crack

In Case (a), we analyse the inclined crack shown in Fig. 16(a). The variations of K_I and K_{II} (normalised by $\bar{p}\sqrt{\pi a}$) with the crack orientation θ are presented in Fig. 17(a). The numerical results are obtained considering ten elements along each crack surface. The responses provided by Liu et al. [71] using an XFEM formulation to extract the SIFs directly are also shown in Fig. 17(a). Good agreement is observed between the solutions determined by IGABEM and XIGABEM and the analytical responses given by Eq. (33). Furthermore, it can be noted that, in general, the results determined here better approximate the analytical results when compared to the XFEM approach. This occurs especially because the boundary integral formulation allows the simulation of the infinite domain, whereas a finite plate was considered in Liu et al. [71], which introduced errors due to the mesh truncation.

Fig. 17(b) shows the curves for the error variation in the SIFs with crack mesh refinement considering $\theta = 30°$, which are similar to the curves obtained for other crack orientations. As in the previous examples, the combination of the enriched formulation with the J-integral significantly improves the convergence rate and the accuracy of the SIFs recovered. On the other hand, the direct method is less accurate than the unenriched IGABEM due to the interaction between the crack tips. However, the errors obtained by the direct approach remain low, with the same order of magnitude observed in the previous example, ranging from 1% down to 0.2%.

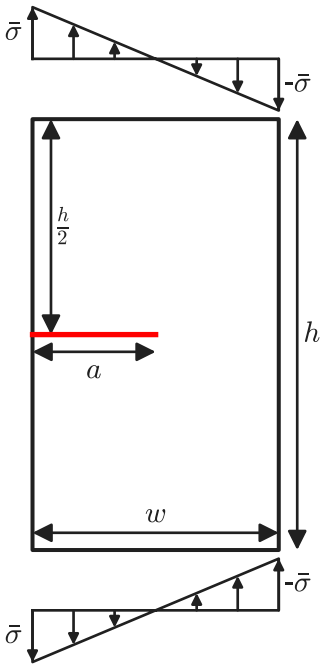

Fig. 13. Rectangular plate with an edge crack under uniform loading.

Although providing higher SIFs errors than the indirect approaches for this problem, the direct method is capable of substantially reducing the analysis time by avoiding the calculation of mechanical fields on internal points. Fig. 18(a) presents the run times obtained by the conventional IGABEM and by the direct and indirect XIGABEM for the different discretisations of the crack surfaces. The execution time values t are normalised by $t_0 = 10.9$ ms, the smallest run time observed that corresponds to the direct XIGABEM for the coarsest mesh. Note that for all meshes, the lowest run times are obtained by the direct approach, followed by the indirect IGABEM and lastly by the indirect XIGABEM. The percentage differences between the processing times are presented in Fig. 18(b), taking the IGABEM results as reference. On average, the direct method is 45% faster than the conventional IGABEM that applies the J-integral to evaluate the SIFs, which demonstrates the advantage of the proposed formulation from the computational cost standpoint. On the other hand, the simultaneous use of the enriched formulation and J-integral increases the processing time by 80% on average, since the enriched integral kernels must be computed both for construction of the system of equations and for definition of the internal quantities — and for this particular problem, the increase tends to be more pronounced since all the elements are enriched. Nevertheless, this increment in computational cost leads to a significant gain in the accuracy of the SIFs, as presented in Fig. 17(b).

Fig. 19 illustrates the interaction between displacement solutions for the two crack tips considering the XIGABEM formulation. The enrichment term provides a deformed shape for each tip considering both tips in isolation, as shown in Fig. 19(b). The addition of the contribution from the NURBS basis functions, depicted in Fig. 19(a), allows the scheme to recover the ellipse-like deformed shape in Fig. 19(c). This is a good illustration of the role that the NURBS basis functions are required to play over enriched portions of the boundary; this role can be viewed as the capturing of the difference between the pure mode behaviour (expressed in the enrichment terms) and the true solution we seek.

Case (b): Circular arc crack

In Case (b), we analyse the circular arc crack presented in Fig. 16(b). The use of the isogeometric analysis is especially beneficial for solving this problem since the NURBS approximation allows the exact representation of the curved crack geometry.

For curved crack paths, the accuracy of the SIFs computed by the interaction integral method is compromised when assuming the asymptotic crack tip solutions as auxiliary fields, unless the integration contour is contracted to the tip to disregard the effect of the curvature of the crack surfaces [72]. On the other hand, the direct method proposed in this paper does not suffer from this drawback since the near-tip solution – which is related to the SIFs obtained by the method – is properly represented by the enrichment term. The application of the direct XIGABEM for the evaluation of the SIFs for the circular arc crack is illustrated by Fig. 20(a), which shows the variation of K_I and K_{II} (normalised by $\bar{p}\sqrt{\pi a}$) for different crack angles 2θ. For the simulations, the crack surfaces are discretised into sixteen elements. Good agreement is attained between the results obtained here and the analytical solutions given by Eq. (34), which demonstrates the accuracy of the proposed method. The results are also in accordance with the numerical solutions obtained by Yan [73] using BEM and by Choi and Cho [74] using isogeometric FEM.

Fig. 20(b) presents the convergence of the SIFs determined by the direct XIGABEM considering different crack angles 2θ. This set of results demonstrates the stability of the method for the analysis of curved cracks. Despite the differences between the convergence patterns when different crack curvatures are considered, note that most of the errors

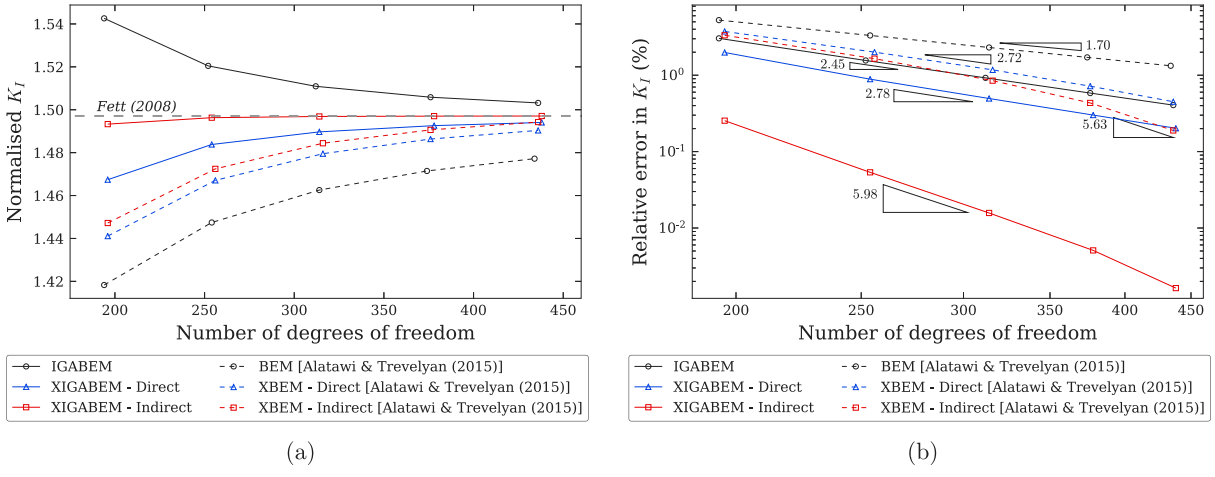

Fig. 14. Variation of (a) mode I SIF (normalised by $\bar{\sigma}\sqrt{\pi a}$) and (b) relative error with the mesh refinement obtained by the present work and by Alatawi and Trevelyan [46]. The reference value for normalised K_I is taken from Fett [68].

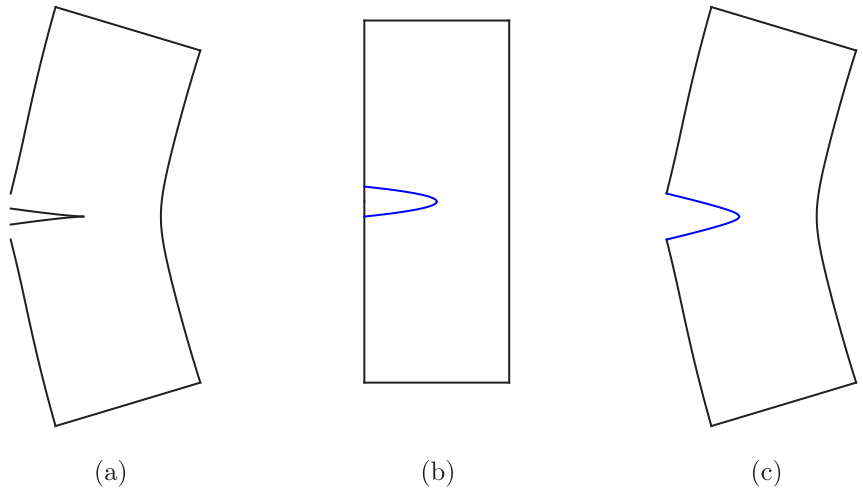

Fig. 15. Deformed shapes considering the contribution from (a) the NURBS basis functions and (b) the enrichment term. (c) Final deformed shape for pure mode I problem, given by the superposition of solutions from (a) and (b). The enriched NURBS are depicted in blue (please refer to the coloured version).

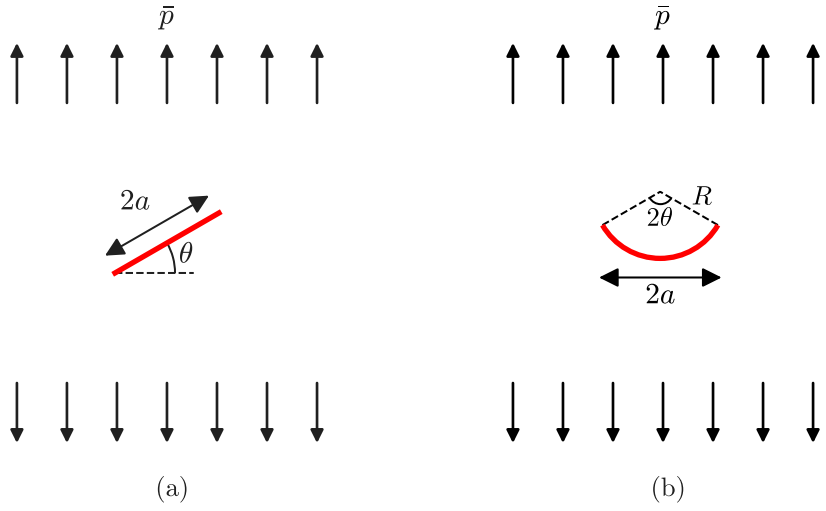

Fig. 16. Cracks in an infinite domain submitted to far-field vertical loading: (a) Inclined crack and (b) circular arc crack.

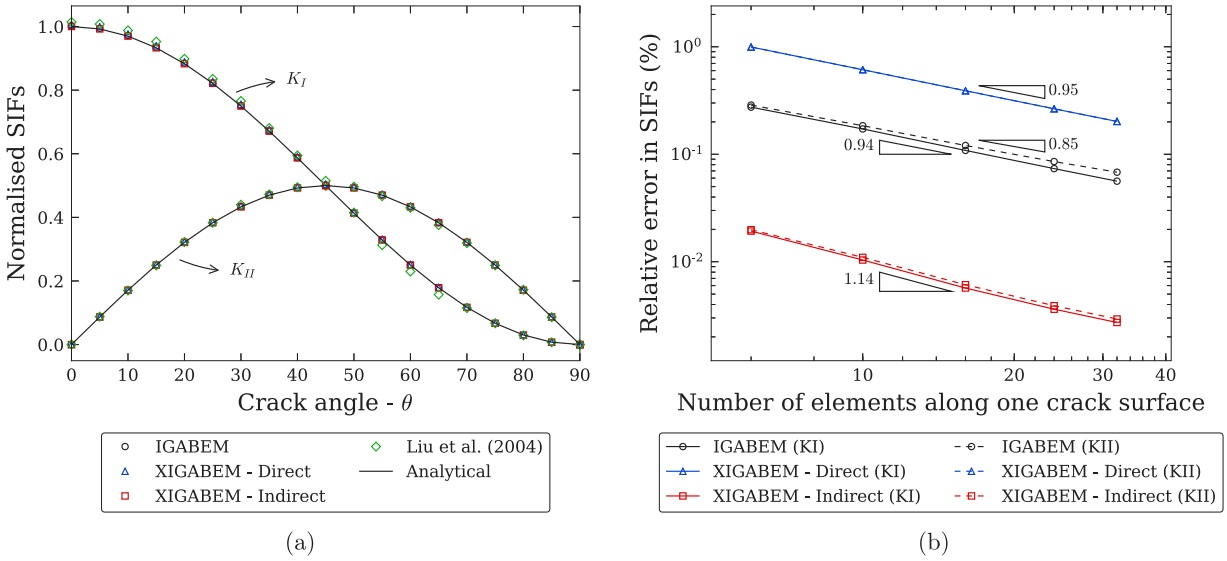

Fig. 17. (a) Results for normalised SIFs for inclined crack considering 10 elements in each crack surface. (b) Relative error evolution with crack mesh refinement.

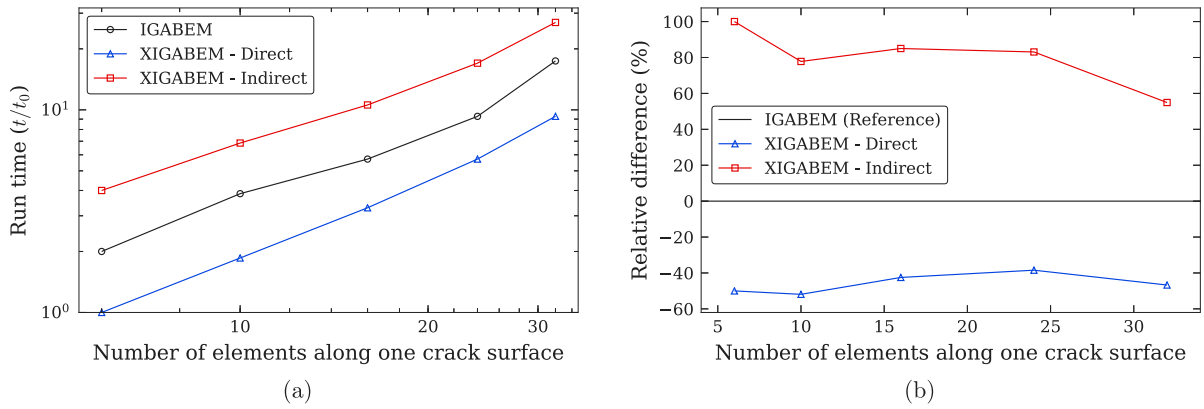

Fig. 18. (a) Variation of execution time with crack mesh refinement. The values are normalised by $t_0 = 10.9$ ms, which is the smallest time observed and corresponds to the run time of the direct XIGABEM for the coarsest discretisation. (b) Relative differences between run times considering the indirect IGABEM results as reference.

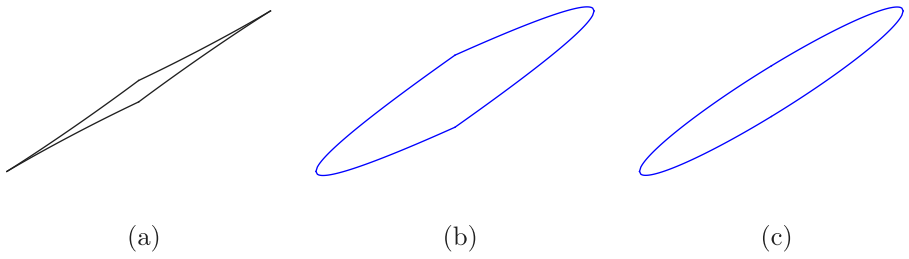

Fig. 19. Deformed shapes for inclined crack ($\theta = 30°$) considering the contribution from (a) the NURBS basis functions and (b) the enrichment term. (c) Final deformed shape for inclined crack, given by the superposition of solutions from (a) and (b). Enriched NURBS are depicted in blue (please refer to the coloured version).

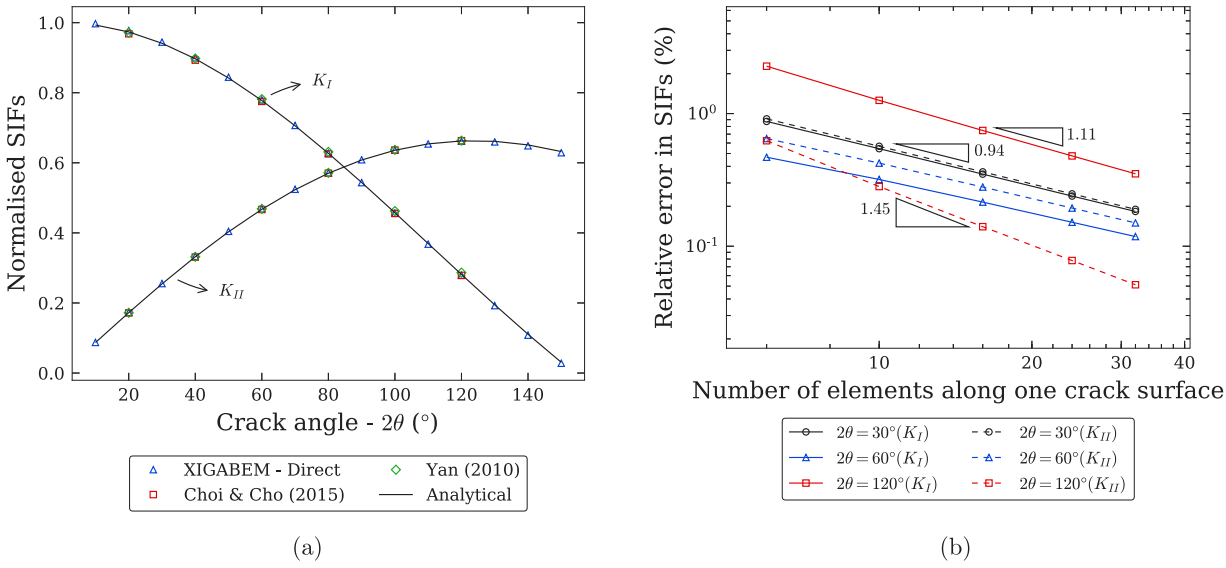

Fig. 20. (a) Results for normalised SIFs for circular arc crack considering 16 elements in each crack surface. (b) Relative error evolution with crack mesh refinement.

are below 1% even for coarse meshes, which is a behaviour similar to Case (a).

The role of each term in the enriched displacement approximation for the solution of the circular arc crack problem is illustrated in Fig. 21. As in the previous examples, the enrichment term (Fig. 21(b)) is responsible for representing the near-tip behaviour, while the NURBS basis (Fig. 21(a)) captures the difference between the asymptotic solution and the real solution of the problem. The superposition of both contributions allows the recovery of the final response depicted in Fig. 21(c).

5.2. Fatigue crack growth

5.2.1. Titanium plate with a central inclined crack

Fig. 22 shows a rectangular titanium plate containing a central crack of length $2a = 13.462$ mm inclined of an angle $\theta = 47°$ with respect to the horizontal direction. The dimensions of the structure are $w = 76.2$ mm and $h = 304.8$ mm. A fatigue test of such a plate was conducted by Pustejovsky [75] considering a loading amplitude $\bar{\sigma}$ ranging from 17.24 to 172.37 MPa. This experiment is reproduced numerically with the XIGABEM model considering the following Paris law parameters : $C = 3.781 \times 10^{-15}$ and $m = 3.81$, with da/dN given in

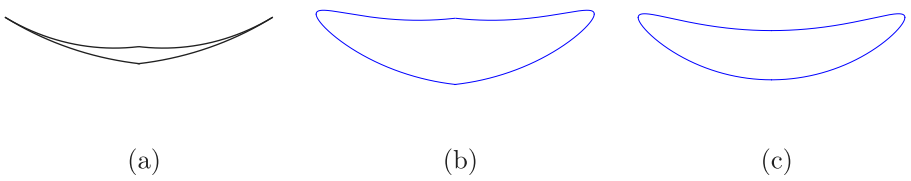

Fig. 21. Deformed shapes for circular arc crack ($2\theta = 60°$) considering the contribution from (a) the NURBS basis functions and (b) the enrichment term. (c) Final deformed shape for curved crack, given by the superposition of solutions from (a) and (b). Enriched NURBS are depicted in blue (please refer to the coloured version).

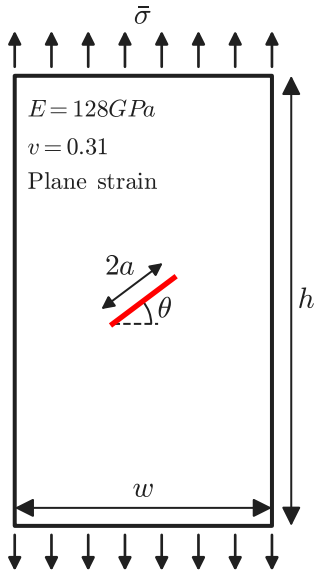

Fig. 22. Rectangular specimen of a titanium plate with a central inclined crack.

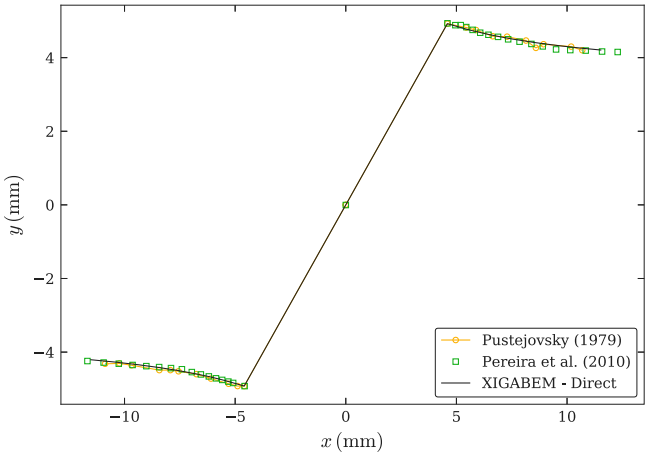

Fig. 23. Comparison between the propagation path obtained by the XIGABEM model considering the direct approach for SIFs extraction and the experimental results determined by Pustejovsky [75]. The numerical solution obtained by Pereira et al. [76] using GFEM is also provided.

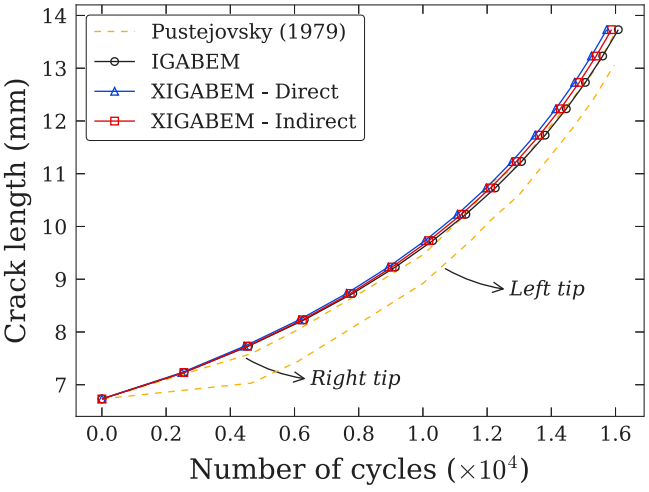

Fig. 24. Crack length evolution with number of load cycles. The solutions obtained experimentally by Pustejovsky [75] are also provided.

mm/cycles and ΔK_{ef} in MPa×mm$^{0.5}$. To perform the numerical analysis, each crack surface is discretised in fifteen elements, while fifty elements are adopted along the external boundary. A crack length increment $\Delta a = 0.5$ mm is used for the fatigue growth, while two elements inserted along each new crack surface.

Fig. 23 shows the propagation path determined by the XIGABEM model considering the direct method for evaluating the SIFs. The experimental result obtained by Pustejovsky [75] and the numerical response provided by Pereira et al. [76] generalised FEM (GFEM) are also depicted in the figure. Good agreement is attained between the solution determined by the proposed enriched formulation with the experimental and numerical results found in the literature.

The crack length evolution with the number of loading cycles is presented in Fig. 24. There is a good correspondence between the unenriched and enriched formulations adopted in the present study. At the end of 14 increments, the fatigue life determined by the numerical approaches is approximately 16 thousand cycles, which agrees particularly well with the experimental results for the right tip given by Pustejovsky [75].

5.2.2. Open spanner

In this example, we explore the advantage of using the isogeometric formulation to deal with geometries taken directly from CAD. For this purpose, we consider the open spanner subjected to a cyclic loading $\bar{p}$ with range $0 \sim 10$, as illustrated in Fig. 25. The knot-vector and the positions of the main control points for the definition of the B-spline representing the external boundary are also presented in the figure. An initial edge flaw with length $a = 0.15$ is located in a region of high stress concentration given by an elastostatic analysis [12]. The geometry of this problem was originally proposed by Simpson et al. [12], and a crack propagation analysis was later conducted by Peng et al. [42].

Here, we perform a fatigue analysis with the proposed XIGABEM formulation considering the following parameters: $C = 10^{-13}$, $m = 2.6$ and $\Delta a = 0.1$. Each crack surface is initially discretised in three elements, and two new elements are added after each crack increment.

Fig. 26 illustrates the deformed shape after ten crack increments determined by the direct XIGABEM model. Good agreement is noted between the crack paths obtained here and the reference solution given by Peng et al. [42]. The variation of the SIF values with crack length is presented in Fig. 27(a). At the initial configuration, the magnitude of K_{II} is significant; however, as the crack grows, the magnitude of K_{II} remains low, and the propagation becomes mode I dominant.

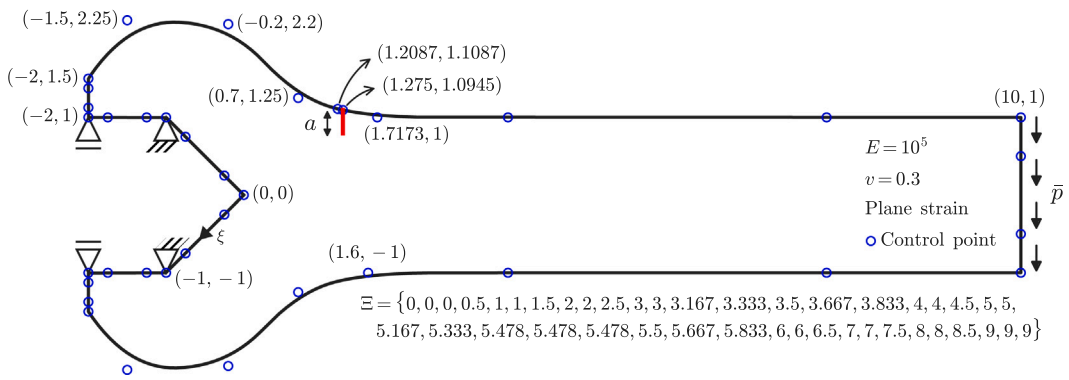

Fig. 25. Open spanner with an edge crack. The repeated knot 5.478 in the knot vector defining the external boundary indicates the position of the crack mouth. Besides, the weights associated with the control points are taken as a unit.

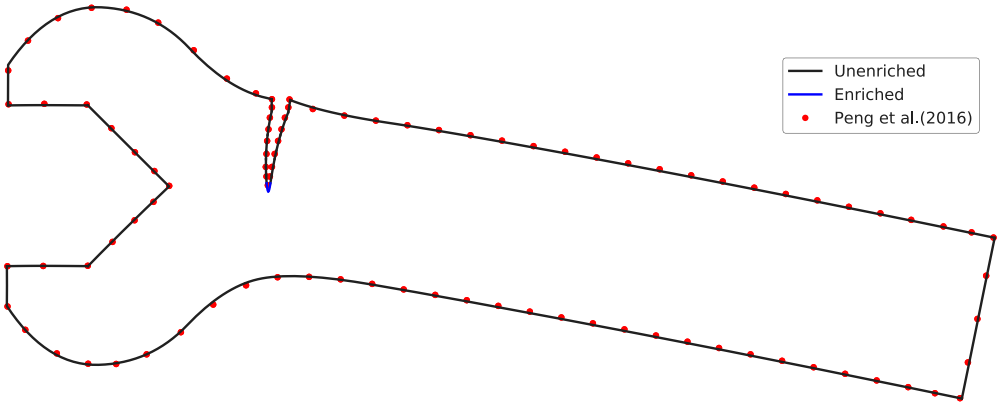

Fig. 26. Deformed shape after ten crack increments obtained with the XIGABEM model considering the direct method for SIF extraction. The segments near the crack tip containing the enrichment term for the displacement approximation are depicted in blue (please refer to the coloured version). The solution provided by Peng et al. [42] is also shown for comparison.

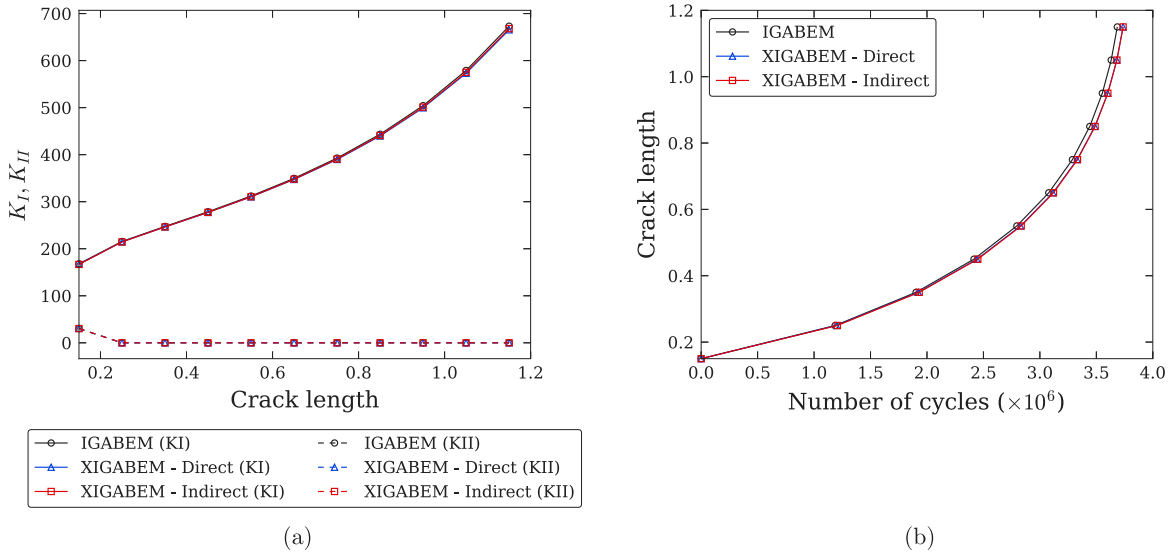

Fig. 27. Variation of (a) SIFs and (b) the number of load cycles with crack evolution.

A small difference can be observed between the values obtained by IGABEM and XIGABEM, a difference also reflected in the results for the evolution of the crack length with the number of load cycles, as shown in Fig. 27(b). For the XIGABEM models, the final configuration is achieved after approximately 3.74 million load cycles, whereas this number is around 3.68 million cycles considering IGABEM.

5.2.3. Perforated plate with an edge crack

Fig. 28 shows a rectangular plate containing two holes of diameter $\phi = 0.4$ and subjected to an uniform cyclic loading $\bar{p}$ with magnitude $0 \sim 10$. The length and height of the structure are $2L$ and L, respectively, with $L = 1$. A vertical crack emanates from the bottom edge and has initial length $a = 0.05$. In this example, we consider different

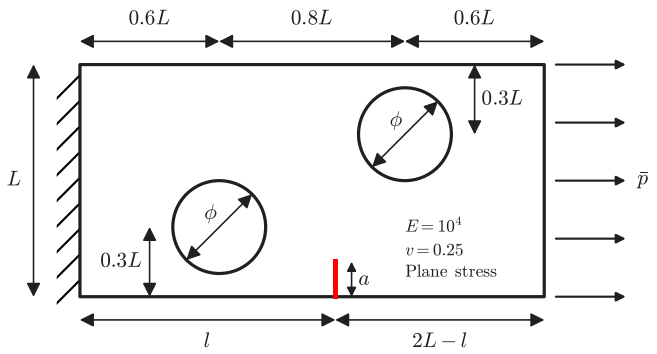

Fig. 28. Tensioned rectangular plate with two holes and an edge crack.

values for l, the parameter defining the initial position of the defect, to assess its effect on the crack path and fatigue life. The following values are adopted: $l = \{0.95, 1.025, 1.1, 1.175, 1.25\}$. Furthermore, we take the parameter values $C = 10^{-10}$, $m = 3.0$ and $\Delta a = 0.025$ for the fatigue analysis.

Figs. 29(a) to 29(e) show the deformed shapes for the different values of l obtained with XIGABEM considering the direct approach for SIF extraction. Figs. 29(a), 29(d) and 29(e) present, respectively, the cases where $l = 0.95$, $l = 1.175$ and $l = 1.25$, in which the crack is attracted to, and ends up intersecting one of the openings. The successive knot insertion to achieve C^{-1} continuity at the intersection point in the NURBS representing the hole is capable of modelling the displacement discontinuity at the crack mouth. In the cases represented by Figs. 29(b) and 29(c), where $l = 1.025$ and $l = 1.1$, respectively, the crack path tends to deviate towards the holes, but then moves away following a direction perpendicular to the applied load. The final crack paths determined in each one of these scenarios are grouped in Fig. 29(f).

The evolution of the crack length with load cycles, for each initial crack position, is illustrated in Fig. 30, where the results obtained by the IGABEM and XIGABEM formulations are compared. The stress concentration caused by the left hole increases the crack growth rate as the initial crack position is moved to the left (lower values of l), decreasing the fatigue life. The responses determined with the different formulations are very similar, differing by less than 1.0%. The final number of load cycles for each case, given in ascending order of l, is approximately: 0.65, 1.27, 2.07, 3.52 and 5.93 million cycles.

To illustrate the reduction in computational cost when considering the proposed direct method, the execution times for the different approaches to simulate the crack growth for $l = 1.1$ are presented in Fig. 31(a). The figure shows the variation of the accumulated run time with the number of degrees of freedom, which are introduced in the numerical models when discretising the new surfaces after each crack extension. The results of processing time are normalised by $t_0 = 93.7$ ms, the smallest time observed among the analyses of the initial configuration, which corresponds to that obtained in the direct XIGABEM. When the proposed direct method is considered, the run times to obtain the responses for each crack configuration are significantly lower than those of the indirect methods. In percentage terms, as presented in Fig. 31(b), the direct XIGABEM is, on average, 40% faster than the conventional IGABEM coupled with the J-integral for computing the SIFs. This result demonstrates the advantage of the proposed formulation since it is able to provide answers with high accuracy, with small differences compared to the indirect methods as presented in Fig. 30, at a significantly lower computational cost. When the indirect XIGABEM is considered for the analysis, the processing time takes, on average, 16% longer than conventional IGABEM due to the consideration of the enriched integral kernels in the formulation. Nevertheless, this increase in computational cost is compensated by very accurate solutions for the SIFs, as demonstrated by the examples in Section 5.1.

5.2.4. Perforated panel with multiple cracks

In this example, we analyse the perforated panel shown in Fig. 32. The structure contains three holes of diameter $\phi = 10$ mm, with cracks of length $a = 3$ mm emanating from the top and bottom of each hole. The length in Fig. 32 is taken as $L = 100$ mm. A cyclic load with components $\bar{p}_x = 9$ MPa and $\bar{p}_y = 1$ MPa is applied to the right edge of the panel, with a stress ratio of zero, while the left edge remains fixed. For the fatigue analysis, the Paris law constants are taken as $C = 10^{-13}$ and $m = 2.6$, assuming da/dN given in mm/cycles and ΔK_{ef} in MPa × mm$^{0.5}$. During the crack growth, the crack length increment for the fastest growing tip is $\Delta a = 1$ mm, with the others growing

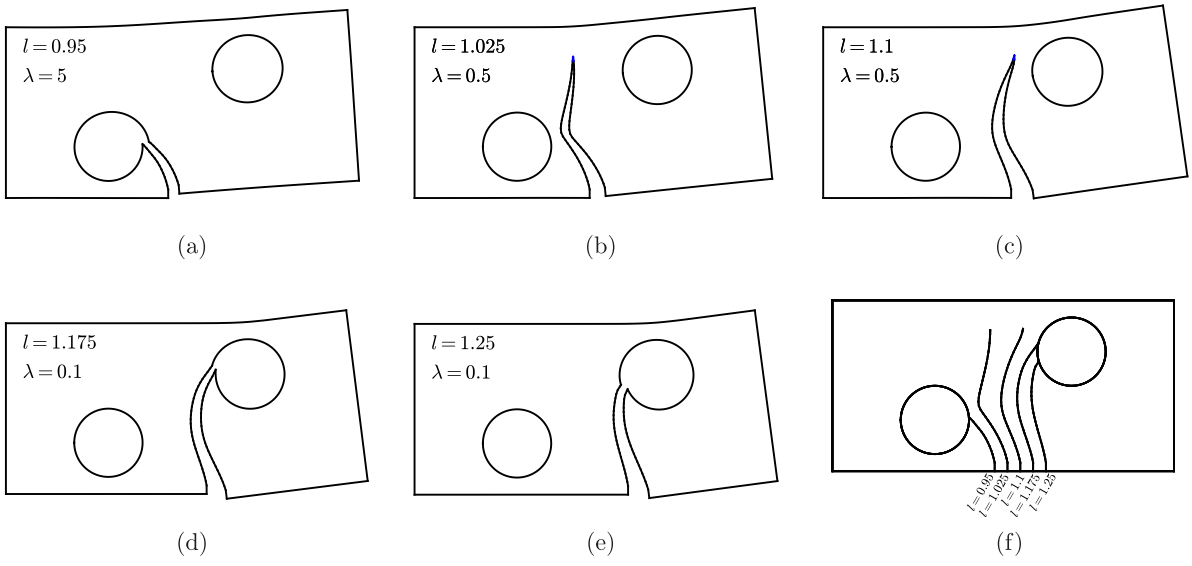

Fig. 29. Deformed shape for the configuration considering (a) $l = 0.95$, (b) $l = 1.025$, (c) $l = 1.1$, (d) $l = 1.175$ and (e) $l = 1.25$. The scale factor λ used in each figure is also indicated. The NURBS segments near the crack tip containing the enrichment term for the displacement approximation are depicted in blue (please refer to the coloured version). Note that in the models where the crack crosses a boundary, the enrichment is removed from the near-tip elements since the analytical square root behaviour no longer exists once the intersection occurs. (f) Crack paths determined for each initial crack position.

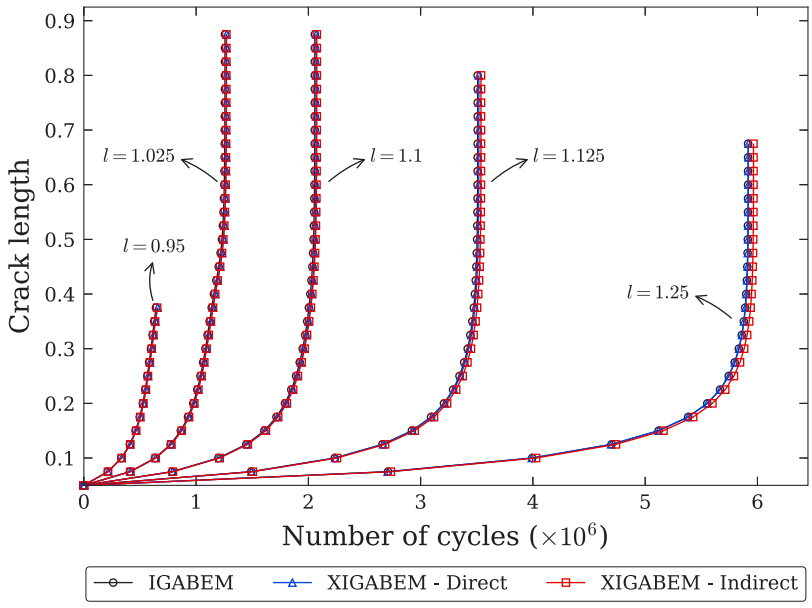

Fig. 30. Crack length evolution determined by the unenriched and enriched formulations considering the different values of l.

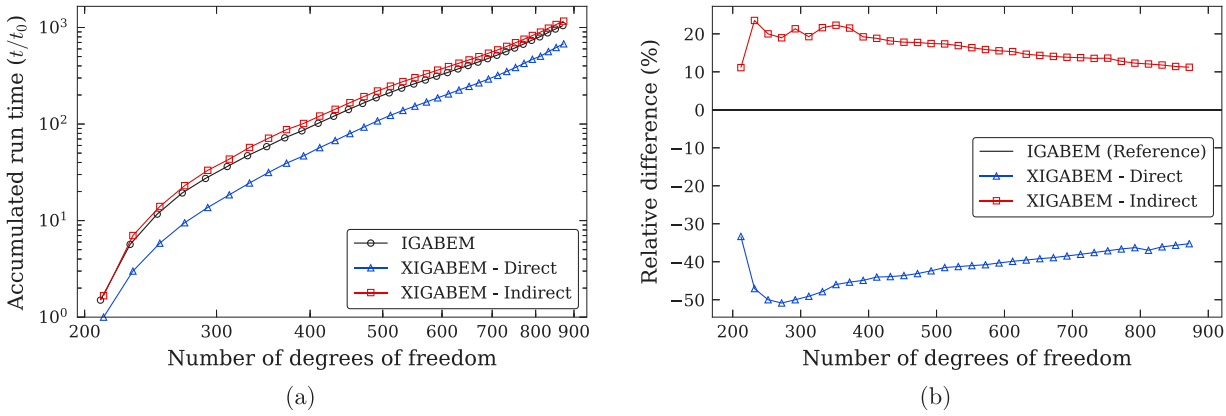

Fig. 31. (a) Accumulated run time to obtain the solution for each crack configuration. The values are normalised by t_0 = 93.7 ms, which is the smallest time observed among the analyses of the initial configuration and corresponds to that obtained in the direct XIGABEM. (b) Relative differences between accumulated run times considering the indirect IGABEM results as reference.

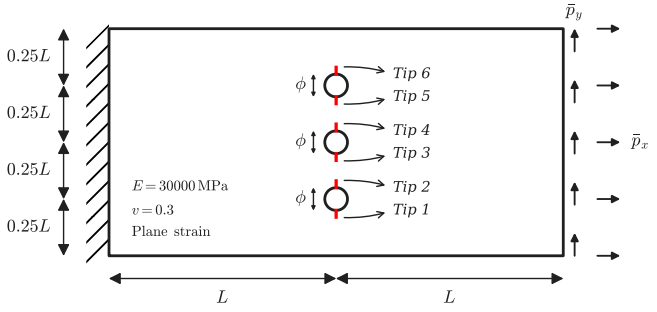

Fig. 32. Perforated panel containing multiple cracks.

proportionally to their respective growth rates. For the initial geometry, each crack surface is discretised with four elements, with a minimum of two elements being added to the new surfaces after propagation.

Fig. 33(a) presents the evolution of ΔK_{ef} for the tips after each crack increment. The results are obtained by XIGABEM considering the direct approach for SIF computation. The curves in the figure can be interpreted in conjunction with the sequence illustrating the crack propagation in Fig. 34. For initial geometries (Fig. 34(a)), tip 1 has the greatest ΔK_{ef}, and consequently the highest growth rate, due to the bending effect in the plate. However, as the cracks start to grow, the stress concentration caused by the interaction between tips 2 and 3 (Fig. 34(b)) soon makes them surpass tip 1 as the most dominant, with both developing similar growth rates. However, the growth at tips 2 and 3 becomes retarded as they start to overlap each other in the classical fashion for opposing cracks (Fig. 34(c)), and tip 1 regains its dominance. At later crack increments, tips 2 and 3 develop small growth rates, whereas tips 4 and 5 move towards each other at faster rates (Fig. 34(d)). As happened for tips 2 and 3, the pair 4 and 5 also experience retardation in their crack growth rates as they overlap (Fig. 34(d)). Tip 1 continues to be the fastest growing tip and moves towards the bottom edge of the panel (Fig. 34(e)), finally intersecting the external boundary. Fig. 34(f) shows the final deformed shape for the structure, in which the discontinuities in the NURBS representing the perforations and the bottom edge are clearly visible.

The history of ΔK_{ef} with crack length is shown in Fig. 33(b). Since tip 1 is dominant for most of the analysis, it develops the largest length. For the interacting cracks – tips 2–3 and tips 4–5 – it can be noted

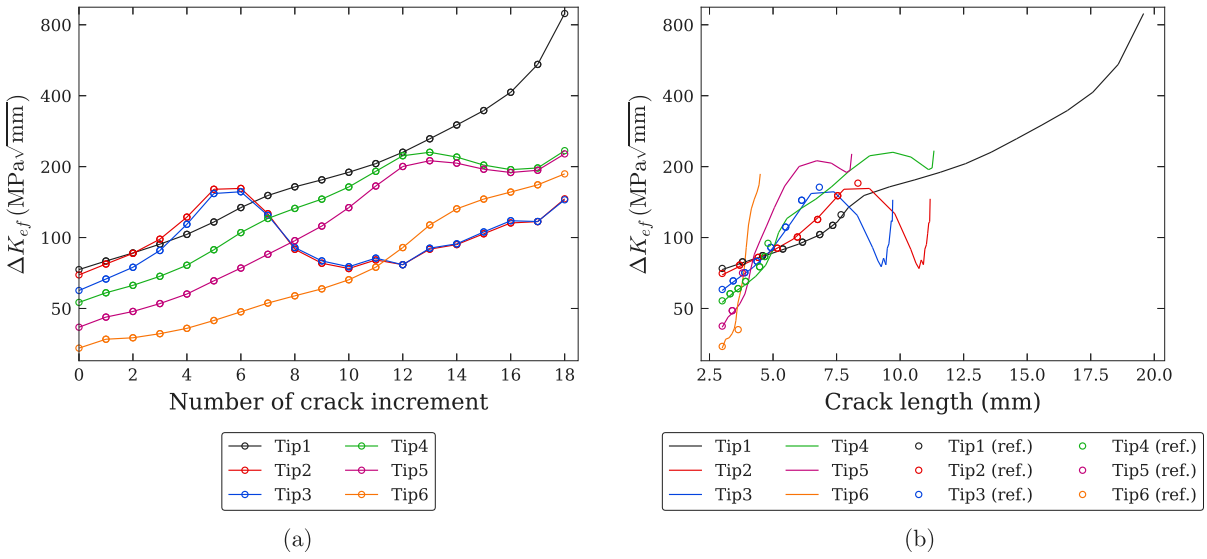

Fig. 33. Variation of ΔK_{ef} with (a) crack increment and (b) crack length.

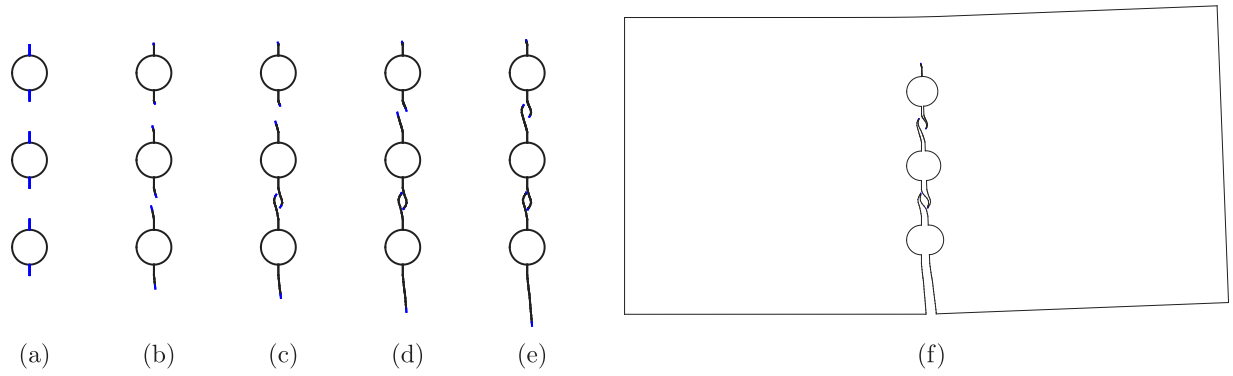

Fig. 34. (a)–(e) Evolution of the crack paths and (f) final deformed shape obtained by the direct XIGABEM formulation. The enriched NURBS segments are depicted in blue (please refer to the coloured version).

that, as they approach each other, the behaviour for the pair is very similar, with the crack positioned towards the bottom of the plate having larger lengths due to the bending effect. The results obtained by Price and Trevelyan [63] using BEM are also given in Fig. 33(b). The reference considered fewer crack increments than the present study, but the solutions provided are in good agreement with the results obtained by XIGABEM.

The incremental evolution of the fatigue crack growth in the perforated panel is shown in Fig. 35. Since this problem contains multiple cracks, with different tips dominating as the analysis progresses, the number of load cycles is related to the number of the crack increment. The dominant tip in each geometry is also indicated. A sudden decrease in the crack growth rate can be seen between increments 6 and 7, after tip 1 regains its dominance. This occurs because the value of ΔK_{ef} in increment 6 (related to tip 2) is greater than the value of ΔK_{ef} in increment 7 (related to tip 1). The solutions obtained by IGABEM and XIGABEM considering the J-integral for SIF evaluation are also shown in Fig. 35 for comparison. Good agreement is observed between these results, demonstrating the accuracy of the direct method in solving problems of multiple fatigue crack propagation.

Finally, Fig. 36(a) presents the accumulated run time for the analysis of each configuration during crack growth. The results obtained by the proposed XIGABEM formulation, considering both the direct and indirect methods for SIF extraction, are compared against those determined by the conventional IGABEM. The execution time values

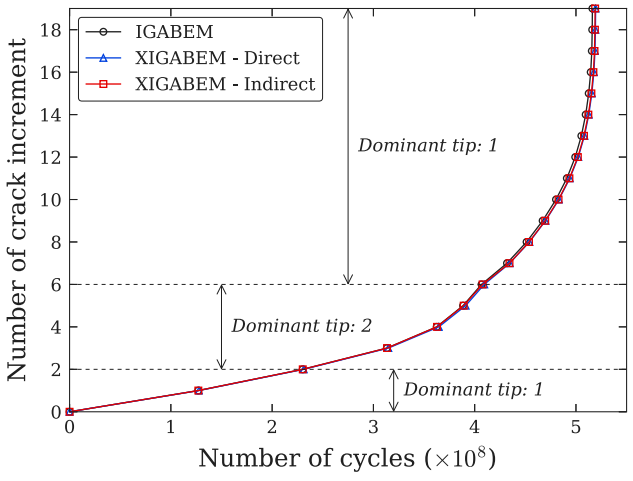

Fig. 35. Incremental fatigue process for the perforated panel determined by the unenriched and enriched formulations.

t are normalised by t_0 = 156.2 ms, which is the time for the analysis of the initial configuration considering the direct XIGABEM approach. As in the previous examples, when the direct approach is considered,

the run times to simulate the crack propagation are considerably lower than when the indirect method based on the J-integral is used for evaluation of the SIFs. Besides, the indirect XIGABEM solutions take slightly longer to obtain compared to the unenriched IGABEM due to the consideration of the enriched integral kernels in the isogeometric formulation. Nonetheless, this small increase in computational cost is accompanied by a large improvement in the accuracy of the SIF solutions, as demonstrated in Section 5.1.

The relative differences in execution times determined by XIGABEM (direct and indirect) compared to IGABEM are shown in Fig. 36(b). In the case of the indirect XIGABEM, the run times are 30% to 40% higher than for the conventional IGABEM at the start of the analysis; however, the absolute values of time are small, in the order of seconds. As the propagation progresses, these differences diminish and stabilise around 15% towards the end of the analysis. For the direct XIGABEM, the time saving compared to the unenriched method is substantial: at the beginning of the analysis, it is around 60% and, at the end, the reduction in computational cost is approximately 50%. It is worth emphasising that the time saving provided by the direct method is higher in this example than in Section 5.2.3. This is due to the fact that now multiple cracks are involved in the analysis and, consequently, the computational cost of using several J-integrals to calculate the SIFs in the indirect method compared to the direct approach is proportionally higher than in the previous example.

This application demonstrates the advantage of the proposed direct XIGABEM for the crack analysis, particularly those involving large-scale problems requiring several computations for the SIFs. Such method is able to significantly decrease the computational cost while the accuracy of the results is ensured.

6. Concluding remarks

An enriched isogeometric boundary element (XIGABEM) formulation for simulating fatigue crack growth was presented. The crack tip functions used for displacement enrichment, associated with the crack tip tying constraint, enabled the stress intensity factors (SIFs) to be computed directly from the system of equations provided by XIGABEM. A key feature of this scheme is the avoidance of computational costly post-processing techniques for SIF computation such as the J-integral, since the SIFs are given as terms in the solution vector. We term this the direct approach, and have shown that it is able to provide SIF values with errors, in most cases, that were lower than those from an unenriched IGABEM formulation, in which the J-integral was applied for SIF extraction. Even when the unenriched IGABEM outperformed the direct XIGABEM approach (inclined crack problem), the errors obtained by the direct approach were satisfactory, being less than 1%. Moreover, the execution time of the direct method was significantly lower than that of the conventional indirect method. Alternatively, for cases in which very high accuracy is required, a J-integral calculation based on the XIGABEM results is able to improve considerably the accuracy and convergence rate for SIF calculations.

The first set of examples clearly demonstrate the accuracy and convergence benefits of the new formulation, and these can be seen in the results shown in Figs. 10, 12, 14 and 17. Besides, the direct approach can also be successfully applied to analyse curved cracks, as illustrated in Case (b) of the last example of the set.

Regarding the fatigue applications, the direct XIGABEM model provided propagation paths, SIF history and fatigue lives in good agreement with experimental and numerical results available in the literature. In general, the solutions given by the direct approach better approximated those found by combining the enriched XIGABEM formulation and the J-integral – which is the most accurate model – when compared to unenriched IGABEM. Additionally, as demonstrated by the last two examples, the run times when the direct approach is considered are substantially lower than those determined when using the indirect J-integral for SIF extraction. Furthermore, an increase in time savings was noted with the number of crack fronts.

The continuity properties of NURBS, related to the multiplicity of repeated knots in the knot vector, was exploited in the development of a C^{-1} continuity strategy that was able to model discontinuities at boundaries intersected by cracks with a trivial modification of the NURBS definition. This strategy was also employed to ensure independence between the basis functions over the new and existing crack surfaces during crack propagation, thus restricting the enriched elements to the NURBS portion defining the crack tip. The independence along the newly created surfaces also facilitated the remeshing process and the corresponding modifications in the system of equations during crack growth.

Finally, the isogeometric boundary element formulation allowed a straightforward integration between CAD and numerical analysis. Unlike domain-based numerical techniques, for which an isogeometric volume description is required, the basis functions adopted in the XIGABEM approach are exactly the same as those used in computational design. The direct link between CAD and analysis is especially useful when dealing with 3D models, where a considerable amount of time can be saved from the mesh generation process. The application of the enriched isogeometric formulation can also be extended to three-dimensional domains, and this is work in progress. Based on the results of the present paper, the prospect of accurate SIF predictions in 3D without the expense of multiple J-integral evaluations is highly appealing.

Acknowledgements

Sponsorship of this research project by the São Paulo State Foundation for Research (FAPESP), project numbers 2016/23649-0 and 2019/03340-3, is greatly appreciated. This study was also financed in part by the Coordenação de Aperfeiçoamento de Pessoal de Nível Superior - Brasil (CAPES) - Finance Code 001.

Appendix A. NURBS basis derivatives

The derivative of order k of NURBS basis functions may be computed from:

$$R_{i,p}^{(k)}(\xi) = \frac{d^k}{d\xi^k} R_{i,p}(\xi) = \frac{w_i N_{i,p}^{(k)}(\xi) - \sum_{l=1}^{k} \left[\binom{k}{l} \sum_{j=1}^{n} N_{j,p}^{(l)}(\xi) w_j R_{i,p}^{(k-l)}(\xi) \right]}{\sum_{j=1}^{n} N_{j,p}(\xi) w_j} \tag{A.1}$$

where $\binom{k}{l} = \frac{k!}{l!(k-l)!}$ and:

$$N_{i,p}^{(k)}(\xi) = \frac{d^k}{d\xi^k} N_{i,p}(\xi) = p \left(\frac{N_{i,p-1}^{(k-1)}(\xi)}{\xi_{i+p} - \xi_i} - \frac{N_{i+1,p-1}^{(k-1)}(\xi)}{\xi_{i+p+1} - \xi_{i+1}} \right) \tag{A.2}$$

Appendix B. Fundamental solutions

Considering a point-force problem, the fundamental solutions in the DBIE (7) are given by:

$$U_{ij}^{*}(\mathbf{x}', \mathbf{x}) = \frac{1}{8\pi\mu(1-\nu)} \left[(3-4\nu) \ln\left(\frac{1}{r}\right) \delta_{ij} + r_{,i} r_{,j} \right] \tag{B.1}$$

$$P_{ij}^{*}(\mathbf{x}', \mathbf{x}) = -\frac{1}{4\pi(1-\nu) r} \times \left\{ (1-2\nu)\left(r_{,j} n_i - r_{,i} n_j\right) + \frac{\partial r}{\partial n} \left[(1-2\nu)\delta_{ij} + 2 r_{,i} r_{,j} \right] \right\} \tag{B.2}$$

with $r := \|\mathbf{x}' - \mathbf{x}\|$ representing the distance between the source point $\mathbf{x}'$ and the field point $\mathbf{x}$; n_j are the components of the outward unit normal vector at $\mathbf{x}$ and ν is Poisson's ratio of the material.

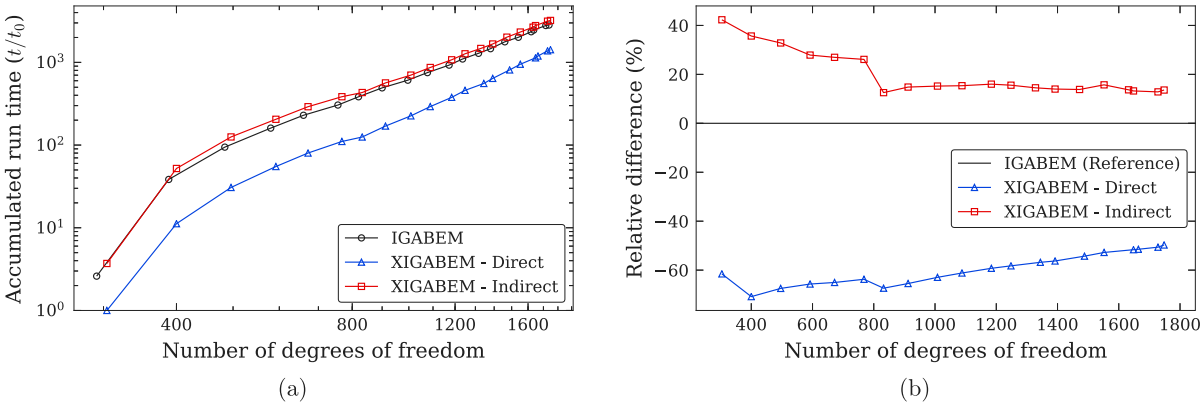

Fig. 36. (a) Accumulated run time to obtain the solution for each crack configuration. The values are normalised by $t_0 = 156.2$ ms, which is the smallest time observed for the analysis of the initial configuration and corresponds to the run time of the direct XIGABEM. (b) Relative differences between accumulated run times considering the indirect IGABEM results as reference.

Regarding the TBIE (8), the fundamental solutions D^*_{kij} and S^*_{kij} are obtained from the derivatives of U^*_{ij} and P^*_{ij}, respectively, and their expressions are:

$$D^*_{kij}(\mathbf{x}',\mathbf{x}) = \frac{1}{4\pi(1-\nu)r}\left[(1-2\nu)\left(r_{,i}\delta_{jk} + r_{,j}\delta_{ik} - r_{,k}\delta_{ij}\right) + 2r_{,i}r_{,j}r_{,k}\right] \tag{B.3}$$

$$S^*_{kij}(\mathbf{x}',\mathbf{x}) = \frac{\mu}{2\pi(1-\nu)r^2}\left\{2\frac{\partial r}{\partial n}\left[(1-2\nu)r_{,k}\delta_{ij} + \nu\left(r_{,i}\delta_{jk} + r_{,j}\delta_{ik}\right) - 4r_{,i}r_{,j}r_{,k}\right] + \right. \tag{B.4}$$
$$\left. +2\nu\left(n_i r_{,j}r_{,k} + n_j r_{,i}r_{,k}\right) + (1-2\nu)\left(2n_k r_{,i}r_{,j} + n_i\delta_{jk} + n_j\delta_{ik}\right) - (1-4\nu)n_k\delta_{ij}\right\}$$

where $\mu = \frac{E}{2(1+\nu)}$ is the shear modulus of the material, with E being the Young's modulus.

The above fundamental solutions are valid for plane strain conditions. For plane stress problems, these expressions must be used considering the corrected values for Young's modulus $\bar{E} = E\left[1 - \left(\frac{\nu}{1+\nu}\right)^2\right]$ and Poisson's ratio $\bar{\nu} = \frac{\nu}{1+\nu}$.

Appendix C. Evaluation of singular integrands

C.1. Conventional integrands

When integrating an element that contains the source point, the strongly singular and hypersingular integrals arising in the boundary integral equations are evaluated with the SSM. For this purpose, we firstly define the following auxiliary coordinate:

$$\zeta(\hat{\xi},\hat{\xi}') = J^e(\hat{\xi}')\left(\hat{\xi} - \hat{\xi}'\right) \tag{C.1}$$

where $\hat{\xi} \in [-1,1]$ is the non-dimensional coordinate in the parent space, $\hat{\xi}'$ is the parameter at the source point and $J^e(\hat{\xi}')$ is the Jacobian evaluated at the source point.

The kernel P^{em}_{ij} (17) can be rewritten as:

$$P^{em}_{ij} = \int\!\!\!\!\!\!-_{-1}^{1} \frac{\bar{P}^*_{ij}(\hat{\xi},\hat{\xi}')}{r(\hat{\xi},\hat{\xi}')}\phi^{em}(\hat{\xi})J^e(\hat{\xi})d\hat{\xi} \tag{C.2}$$

where $\bar{P}^*_{ij} = rP^*_{ij}$ is the regular part of the traction fundamental solution. P^{em}_{ij} can be regularised by adding and subtracting a kernel with the same order of singularity as follows:

$$P^{em}_{ij} = \int_{-1}^{1} \frac{\bar{P}^*_{ij}(\hat{\xi},\hat{\xi}')}{r(\hat{\xi},\hat{\xi}')}\phi^{em}(\hat{\xi})J^e(\hat{\xi}) - \frac{\bar{P}^*_{ij}(\hat{\xi}')}{\zeta(\hat{\xi},\hat{\xi}')}\phi^{em}(\hat{\xi}')J^e(\hat{\xi}')d\hat{\xi}$$
$$\int\!\!\!\!\!\!-_{-1}^{1} \frac{\bar{P}^*_{ij}(\hat{\xi}')}{\zeta(\hat{\xi},\hat{\xi}')}\phi^{em}(\hat{\xi}')J^e(\hat{\xi}')d\hat{\xi} \tag{C.3}$$

where $\bar{P}^*_{ij}(\hat{\xi}')$ is determined from $\bar{P}^*_{ij}(\hat{\xi},\hat{\xi}')$ when $\hat{\xi} \to \hat{\xi}'$. Substituting the definition of ζ (C.1) in Eq. (C.3) results in:

$$P^{em}_{ij} = \int_{-1}^{1} \frac{\bar{P}^*_{ij}(\hat{\xi},\hat{\xi}')}{r(\hat{\xi},\hat{\xi}')}\phi^{em}(\hat{\xi})J^e(\hat{\xi}) - \frac{\bar{P}^*_{ij}(\hat{\xi}')}{\hat{\xi}-\hat{\xi}'}\phi^{em}(\hat{\xi}')d\hat{\xi} + \bar{P}^*_{ij}(\hat{\xi}')\phi^{em}(\hat{\xi}')CPV \tag{C.4}$$

The first integral on the right-hand side of Eq. (C.4) is regular and can be computed with standard Gauss–Legendre quadrature. The last term contains the Cauchy principal value computed analytically as follows:

$$CPV = \int\!\!\!\!\!\!-_{-1}^{1} \frac{1}{\hat{\xi}-\hat{\xi}'}d\hat{\xi} = \ln\left|\frac{1-\hat{\xi}'}{1+\hat{\xi}'}\right| \tag{C.5}$$

Regarding the TBIE, the kernel D^{em}_{kij} (22) can be evaluated in a similar manner to P^{em}_{ij} since both have the same order of singularity $\mathcal{O}(r^{-1})$. For S^{em}_{kij} (21), it can be firstly rewritten as:

$$S^{em}_{kij} = \int\!\!\!\!\!\!=_{-1}^{1} \frac{\bar{S}^*_{kij}(\hat{\xi},\hat{\xi}')}{r^2(\hat{\xi},\hat{\xi}')}\phi^{em}(\hat{\xi})J^e(\hat{\xi})d\hat{\xi} \tag{C.6}$$

where $\bar{S}^*_{kij} = r^2S^*_{kij}$ is the regular part of the fundamental solution.

The integrand in Eq. (C.6) can be regularised by the SSM considering the first-order Taylor expansion around $\hat{\xi}'$ for the shape functions, resulting in:

$$S^{em}_{kij} = \int_{-1}^{1} \frac{\bar{S}^*_{kij}(\hat{\xi},\hat{\xi}')}{r^2(\hat{\xi},\hat{\xi}')}\phi^{em}(\hat{\xi})J^e(\hat{\xi})$$
$$- \frac{\bar{S}^*_{kij}(\hat{\xi}')}{\zeta^2(\hat{\xi},\hat{\xi}')}\left[\phi^{em}(\hat{\xi}') + \frac{d\phi^{em}}{d\hat{\xi}}(\hat{\xi}')\left(\hat{\xi}-\hat{\xi}'\right)\right]J^e(\hat{\xi}')d\hat{\xi} + \tag{C.7}$$
$$+ \int\!\!\!\!\!\!=_{-1}^{1} \frac{\bar{S}^*_{kij}(\hat{\xi}')}{\zeta^2(\hat{\xi},\hat{\xi}')}\left[\phi^{em}(\hat{\xi}') + \frac{d\phi^{em}}{d\hat{\xi}}(\hat{\xi}')\left(\hat{\xi}-\hat{\xi}'\right)\right]J^e(\hat{\xi}')d\hat{\xi}$$

where $\bar{S}^*_{kij}(\hat{\xi}')$ is obtained from $\bar{S}^*_{kij}(\hat{\xi},\hat{\xi}')$ when $\hat{\xi} \to \hat{\xi}'$. Using Eq. (C.1) in Eq. (C.7) results in:

$$S^{em}_{kij} = \int_{-1}^{1} \frac{\bar{S}^*_{kij}(\hat{\xi},\hat{\xi}')}{r^2(\hat{\xi},\hat{\xi}')}\phi^{em}(\hat{\xi})J^e(\hat{\xi})$$
$$- \frac{\bar{S}^*_{kij}(\hat{\xi}')}{J^e(\hat{\xi}')\left(\hat{\xi}-\hat{\xi}'\right)}\left[\frac{\phi^{em}(\hat{\xi}')}{\left(\hat{\xi}-\hat{\xi}'\right)} + \frac{d\phi^{em}}{d\hat{\xi}}(\hat{\xi}')\right]d\hat{\xi} + \tag{C.8}$$
$$+ \frac{\bar{S}^*_{kij}(\hat{\xi}')}{J^e(\hat{\xi}')}\left[\phi^{em}(\hat{\xi}')HFP + \frac{d\phi^{em}}{d\hat{\xi}}(\hat{\xi}')CPV\right]$$

Again, the first integral on the right-hand side of Eq. (C.8) can be evaluated numerically with Gauss–Legendre quadrature. The last term contains the Cauchy principal value presented in Eq. (C.5) and also the

Hadamard finite part given by:

$$HFP = \neq\!\!\!\!\int_{-1}^{1} \frac{1}{\left(\hat{\xi}-\hat{\xi}'\right)^2} d\hat{\xi} = -\frac{1}{1-\hat{\xi}'} - \frac{1}{1+\hat{\xi}'} \tag{C.9}$$

C.2. Enriched integrands

The SSM can also be used to evaluate the enriched kernels $\tilde{P}^{e\lambda}_{iM}$ and $\tilde{S}^{e\lambda}_{ijM}$ for elements containing the source point. In this case, the equations obtained are similar to Eqs. (C.4) and (C.8), respectively, since the enrichment functions do not modify the order of singularity of the integrands. To define the expressions to compute the singular kernels, the shape functions $\phi^{em}(\hat{\xi})$ are simply replaced by the enrichment term $T^{\lambda}_{jk}\psi_{kM}(\mathbf{x}^{\lambda},\mathbf{x}(\hat{\xi}))$. Hence, for $\tilde{P}^{e\lambda}_{iM}$ we obtain:

$$\tilde{P}^{e\lambda}_{iM} = \int_{-1}^{1} \frac{\bar{P}^{*}_{ij}(\hat{\xi},\hat{\xi}')}{r(\hat{\xi},\hat{\xi}')} T^{\lambda}_{jk}\psi_{kM}(\mathbf{x}^{\lambda},\mathbf{x}(\hat{\xi}))J^{e}(\hat{\xi}) - \frac{\bar{P}^{*}_{ij}(\hat{\xi}')}{\hat{\xi}-\hat{\xi}'} T^{\lambda}_{jk}\psi_{kM}(\mathbf{x}^{\lambda},\mathbf{x}(\hat{\xi}'))d\hat{\xi} + \tag{C.10}$$

$$+ \bar{P}^{*}_{ij}(\hat{\xi}')T^{\lambda}_{jk}\psi_{kM}(\mathbf{x}^{\lambda},\mathbf{x}(\hat{\xi}'))CPV$$

For $\tilde{S}^{e\lambda}_{ijM}$, the following expression is derived after applying the SSM:

$$\begin{aligned}\tilde{S}^{e\lambda}_{ijM} = &\int_{-1}^{1} \frac{\bar{S}^{*}_{kij}(\hat{\xi},\hat{\xi}')}{r^2(\hat{\xi},\hat{\xi}')} T^{\lambda}_{kp}\psi_{pM}(\mathbf{x}^{\lambda},\mathbf{x}(\hat{\xi}))J^{e}(\hat{\xi}) \\ &- \frac{\bar{S}^{*}_{kij}(\hat{\xi}')T^{\lambda}_{kp}}{J^{e}(\hat{\xi}')\left(\hat{\xi}-\hat{\xi}'\right)}\left[\frac{\psi_{pM}(\mathbf{x}^{\lambda},\mathbf{x}(\hat{\xi}'))}{\left(\hat{\xi}-\hat{\xi}'\right)} + \frac{d\psi_{pM}}{d\hat{\xi}}(\mathbf{x}^{\lambda},\mathbf{x}(\hat{\xi}'))\right] d\hat{\xi} + \\ &+ \frac{\bar{S}^{*}_{kij}(\hat{\xi}')T^{\lambda}_{kp}}{J^{e}(\hat{\xi}')}\left[\psi^{\lambda}_{pM}(\mathbf{x}^{\lambda},\mathbf{x}(\hat{\xi}'))HFP + \frac{d\psi_{pM}}{d\hat{\xi}}(\mathbf{x}^{\lambda},\mathbf{x}(\hat{\xi}'))CPV\right]\end{aligned} \tag{C.11}$$

in which the derivative $\frac{d\psi^{\lambda}_{pM}}{d\hat{\xi}}$ can be determined by applying the chain rule as follows:

$$\frac{d\psi^{\lambda}_{pM}}{d\hat{\xi}} = \frac{\partial\psi_{pM}}{\partial\rho}\frac{\partial\rho}{\partial\hat{\xi}} + \frac{\partial\psi_{pM}}{\partial\theta}\frac{\partial\theta}{\partial\hat{\xi}} \tag{C.12}$$

If the parameter θ is kept constant along the crack surfaces, as considered in the present study, the last term of Eq. (C.12) vanishes.

Appendix D. Williams first-order expansion

According to Williams [56], the first-order solution for the displacement components near a crack tip is expressed in terms of the SIFs as:

$$\left\{\begin{array}{c} u_1 \\ u_2 \end{array}\right\} = \frac{1}{2\mu}\sqrt{\frac{\rho}{2\pi}}\left[\begin{array}{cc} \cos\left(\frac{\theta}{2}\right)(\kappa-\cos\theta) & \sin\left(\frac{\theta}{2}\right)(\kappa+2+\cos\theta) \\ \sin\left(\frac{\theta}{2}\right)(\kappa-\cos\theta) & -\cos\left(\frac{\theta}{2}\right)(\kappa-2+\cos\theta) \end{array}\right] \times \left\{\begin{array}{c} K_I \\ K_{II} \end{array}\right\} \tag{D.1}$$

References

[1] Hughes T, Cottrell J, Bazilevs Y. Isogeometric analysis: CAD, finite elements, NURBS, exact geometry and mesh refinement. Comput Methods Appl Mech Engrg 2005;194(39–41):4135–95. http://dx.doi.org/10.1016/j.cma.2004.10.008.

[2] Bazilevs Y, Calo V, Cottrell J, Evans J, Hughes T, Lipton S, et al. Isogeometric analysis using T-splines. Comput Methods Appl Mech Engrg 2010;199(5–8):229–63. http://dx.doi.org/10.1016/j.cma.2009.02.036.

[3] Cottrell J, Reali A, Bazilevs Y, Hughes T. Isogeometric analysis of structural vibrations. Comput Methods Appl Mech Engrg 2006;195(41–43):5257–96. http://dx.doi.org/10.1016/j.cma.2005.09.027.

[4] Cottrell JA, Hughes TJ, Bazilevs Y. Isogeometric analysis: Toward integration of CAD and FEA. John Wiley & Sons; 2009.

[5] Kim H-J, Seo Y-D, Youn S-K. Isogeometric analysis for trimmed CAD surfaces. Comput Methods Appl Mech Engrg 2009;198(37–40):2982–95. http://dx.doi.org/10.1016/j.cma.2009.05.004.

[6] Benson D, Bazilevs Y, Hsu M, Hughes T. Isogeometric shell analysis: The Reissner–Mindlin shell. Comput Methods Appl Mech Engrg 2010;199(5–8):276–89. http://dx.doi.org/10.1016/j.cma.2009.05.011.

[7] Borden MJ, Scott MA, Evans JA, Hughes TJR. Isogeometric finite element data structures based on Bézier extraction of NURBS. Internat J Numer Methods Engrg 2010;87(1–5):15–47. http://dx.doi.org/10.1002/nme.2968.

[8] Verhoosel CV, Scott MA, de Borst R, Hughes TJR. An isogeometric approach to cohesive zone modeling. Internat J Numer Methods Engrg 2010;87(1–5):336–60. http://dx.doi.org/10.1002/nme.3061.

[9] Scott MA, Borden MJ, Verhoosel CV, Sederberg TW, Hughes TJ. Isogeometric finite element data structures based on Bézier extraction of T-splines. Internat J Numer Methods Engrg 2011;88(2):126–56. http://dx.doi.org/10.1002/nme.3167.

[10] Akhras HA, Elguedj T, Gravouil A, Rochette M. Towards an automatic isogeometric analysis suitable trivariate models generation–application to geometric parametric analysis. Comput Methods Appl Mech Engrg 2017;316:623–45. http://dx.doi.org/10.1016/j.cma.2016.09.030.

[11] Politis C, Ginnis AI, Kaklis PD, Belibassakis K, Feurer C. An isogeometric BEM for exterior potential-flow problems in the plane. In: 2009 SIAM/ACM Joint conference on geometric and physical modeling on - SPM 09. ACM Press; 2009, http://dx.doi.org/10.1145/1629255.1629302.

[12] Simpson R, Bordas S, Trevelyan J, Rabczuk T. A two-dimensional isogeometric boundary element method for elastostatic analysis. Comput Methods Appl Mech Engrg 2012;209–212:87–100. http://dx.doi.org/10.1016/j.cma.2011.08.008.

[13] Simpson R, Bordas S, Lian H, Trevelyan J. An isogeometric boundary element method for elastostatic analysis: 2D implementation aspects. Comput Struct 2013;118:2–12. http://dx.doi.org/10.1016/j.compstruc.2012.12.021.

[14] Beer G, Marussig B, Duenser C. Isogeometric boundary element method for the simulation of underground excavations. GÉOtechnique Lett 2013;3(3):108–11. http://dx.doi.org/10.1680/geolett.13.00009.

[15] Beer G, Duenser C. Advanced 3-D boundary element analysis of underground excavations. Comput Geotech 2018;101:196–207. http://dx.doi.org/10.1016/j.compgeo.2018.05.005.

[16] Simpson R, Scott M, Taus M, Thomas D, Lian H. Acoustic isogeometric boundary element analysis. Comput Methods Appl Mech Engrg 2014;269:265–90. http://dx.doi.org/10.1016/j.cma.2013.10.026.

[17] Coox L, Atak O, Vandepitte D, Desmet W. An isogeometric indirect boundary element method for solving acoustic problems in open-boundary domains. Comput Methods Appl Mech Engrg 2017;316:186–208. http://dx.doi.org/10.1016/j.cma.2016.05.039.

[18] Sun Y, Trevelyan J, Hattori G, Lu C. Discontinuous isogeometric boundary element (IGABEM) formulations in 3D automotive acoustics. Eng Anal Bound Elem 2019;105:303–11. http://dx.doi.org/10.1016/j.enganabound.2019.04.011.

[19] Lian H, Kerfriden P, Bordas S. Shape optimization directly from CAD: An isogeometric boundary element approach using T-splines. Comput Methods Appl Mech Engrg 2017;317:1–41. http://dx.doi.org/10.1016/j.cma.2016.11.012.

[20] Sun S, Yu T, Nguyen T, Atroshchenko E, Bui T. Structural shape optimization by IGABEM and particle swarm optimization algorithm. Eng Anal Bound Elem 2018;88:26–40. http://dx.doi.org/10.1016/j.enganabound.2017.12.007.

[21] Oliveira HL, Andrade HC, Leonel ED. An isogeometric boundary element approach for topology optimization using the level set method. Appl Math Model 2020;84:536–53. http://dx.doi.org/10.1016/j.apm.2020.03.047.

[22] Gong Y, Dong C, Qin X. An isogeometric boundary element method for three dimensional potential problems. J Comput Appl Math 2017;313:454–68. http://dx.doi.org/10.1016/j.cam.2016.10.003.

[23] Campos LS, de Albuquerque EL, Wrobel LC. An ACA accelerated isogeometric boundary element analysis of potential problems with non-uniform boundary conditions. Eng Anal Bound Elem 2017;80:108–15. http://dx.doi.org/10.1016/j.enganabound.2017.04.004.

[24] An Z, Yu T, Bui TQ, Wang C, Trinh NA. Implementation of isogeometric boundary element method for 2-D steady heat transfer analysis. Adv Eng Softw 2018;116:36–49. http://dx.doi.org/10.1016/j.advengsoft.2017.11.008.

[25] Nguyen B, Tran H, Anitescu C, Zhuang X, Rabczuk T. An isogeometric symmetric Galerkin boundary element method for two-dimensional crack problems. Comput Methods Appl Mech Engrg 2016;306:252–75. http://dx.doi.org/10.1016/j.cma.2016.04.002.

[26] Peng X, Atroshchenko E, Kerfriden P, Bordas S. Isogeometric boundary element methods for three dimensional static fracture and fatigue crack growth. Comput Methods Appl Mech Engrg 2017;316:151–85. http://dx.doi.org/10.1016/j.cma.2016.05.038.

[27] Cordeiro SGF, Leonel ED. Mechanical modelling of three-dimensional cracked structural components using the isogeometric dual boundary element method. Appl Math Model 2018;63:415–44. http://dx.doi.org/10.1016/j.apm.2018.06.042.

[28] Sun F, Dong C, Yang H. Isogeometric boundary element method for crack propagation based on Bézier extraction of NURBS. Eng Anal Bound Elem 2019;99:76–88. http://dx.doi.org/10.1016/j.enganabound.2018.11.010.

[29] Taus M, Rodin GJ, Hughes TJ. Isogeometric analysis of boundary integral equations: High-order collocation methods for the singular and hyper-singular equations. Math Models Methods Appl Sci 2016;26(08):1447–80. http://dx.doi.org/10.1142/s0218202516500354.

[30] Taus M, Rodin GJ, Hughes TJ, Scott MA. Isogeometric boundary element methods and patch tests for linear elastic problems: Formulation, numerical integration, and applications. Comput Methods Appl Mech Engrg 2019;357:112591. http://dx.doi.org/10.1016/j.cma.2019.112591.

[31] Gong Y, Trevelyan J, Hattori G, Dong C. Hybrid nearly singular integration for isogeometric boundary element analysis of coatings and other thin 2D structures. Comput Methods Appl Mech Engrg 2019;346:642–73. http://dx.doi.org/10.1016/j.cma.2018.12.019.

[32] Melenk J, Babuska I. The partition of unity finite element method: Basic theory and applications. Comput Methods Appl Mech Engrg 1996;139(1–4):289–314. http://dx.doi.org/10.1016/s0045-7825(96)01087-0.

[33] Babuska I, Melenk J. The partition of unity method. Internat J Numer Methods Engrg 1997;40(4):727–58. http://dx.doi.org/10.1002/(sici)1097-0207(19970228)40:4<727::aid-nme86>3.0.co;2-n.

[34] Belytschko T, Black T. Elastic crack growth in finite elements with minimal remeshing. Internat J Numer Methods Engrg 1999;45(5):601–20. http://dx.doi.org/10.1002/(sici)1097-0207(19990620)45:5<601::aid-nme598>3.0.co;2-s.

[35] Benson DJ, Bazilevs Y, Luycker ED, Hsu MC, Scott M, Hughes TJR, et al. A generalized finite element formulation for arbitrary basis functions: From isogeometric analysis to XFEM. Internat J Numer Methods Engrg 2010;765–85. http://dx.doi.org/10.1002/nme.2864.

[36] Luycker ED, Benson DJ, Belytschko T, Bazilevs Y, Hsu MC. X-FEM in isogeometric analysis for linear fracture mechanics. Internat J Numer Methods Engrg 2011;87(6):541–65. http://dx.doi.org/10.1002/nme.3121.

[37] Ghorashi SS, Valizadeh N, Mohammadi S. Extended isogeometric analysis for simulation of stationary and propagating cracks. Internat J Numer Methods Engrg 2011;89(9):1069–101. http://dx.doi.org/10.1002/nme.3277.

[38] Nguyen VP, Anitescu C, Bordas SP, Rabczuk T. Isogeometric analysis: An overview and computer implementation aspects. Math Comput Simulation 2015;117:89–116. http://dx.doi.org/10.1016/j.matcom.2015.05.008.

[39] Singh S, Singh I, Mishra B, Bhardwaj G, Bui T. A simple, efficient and accurate Bézier extraction based T-spline XIGA for crack simulations. Theor Appl Fract Mech 2017;88:74–96. http://dx.doi.org/10.1016/j.tafmec.2016.12.002.

[40] Peake M, Trevelyan J, Coates G. Extended isogeometric boundary element method (XIBEM) for two-dimensional Helmholtz problems. Comput Methods Appl Mech Engrg 2013;259:93–102. http://dx.doi.org/10.1016/j.cma.2013.03.016.

[41] Peake M, Trevelyan J, Coates G. Extended isogeometric boundary element method (XIBEM) for three-dimensional medium-wave acoustic scattering problems. Comput Methods Appl Mech Engrg 2015;284:762–80. http://dx.doi.org/10.1016/j.cma.2014.10.039.

[42] Peng X, Atroshchenko E, Kerfriden P, Bordas SPA. Linear elastic fracture simulation directly from CAD: 2D NURBS-based implementation and role of tip enrichment. Int J Fract 2016;204(1):55–78. http://dx.doi.org/10.1007/s10704-016-0153-3.

[43] Simpson R, Trevelyan J. A partition of unity enriched dual boundary element method for accurate computations in fracture mechanics. Comput Methods Appl Mech Engrg 2011;200(1–4):1–10. http://dx.doi.org/10.1016/j.cma.2010.06.015.

[44] Simpson R, Trevelyan J. Evaluation of J1 and J2 integrals for curved cracks using an enriched boundary element method. Eng Fract Mech 2011;78(4):623–37. http://dx.doi.org/10.1016/j.engfracmech.2010.12.006.

[45] Benzley SE. Representation of singularities with isoparametric finite elements. Internat J Numer Methods Engrg 1974;8(3):537–45. http://dx.doi.org/10.1002/nme.1620080310.

[46] Alatawi I, Trevelyan J. A direct evaluation of stress intensity factors using the extended dual boundary element method. Eng Anal Bound Elem 2015;52:56–63. http://dx.doi.org/10.1016/j.enganabound.2014.11.022.

[47] Rice JR. A path independent integral and the approximate analysis of strain concentration by notches and cracks. J Appl Mech 1968;35(2):379. http://dx.doi.org/10.1115/1.3601206.

[48] Andrade H, Leonel E. An enriched dual boundary element method formulation for linear elastic crack propagation. Eng Anal Bound Elem 2020;121:158–79. http://dx.doi.org/10.1016/j.enganabound.2020.09.007.

[49] Hong H-K, Chen J-T. Derivations of integral equations of elasticity. J Eng Mech 1988;114(6):1028–44. http://dx.doi.org/10.1061/(asce)0733-9399(1988)114:6(1028).

[50] Portela A, Aliabadi MH, Rooke D. The dual boundary element method: Effective implementation for crack problems. Internat J Numer Methods Engrg 1992;33(6):1269–87. http://dx.doi.org/10.1002/nme.1620330611.

[51] Piegl L, Tiller W. The NURBS book. Springer Berlin Heidelberg; 1995, http://dx.doi.org/10.1007/978-3-642-97385-7.

[52] Cox MG. The numerical evaluation of B-splines. IMA J Appl Math 1972;10(2):134–49. http://dx.doi.org/10.1093/imamat/10.2.134.

[53] De Boor C. On calculating with B-splines. J Approx Theory 1972;6(1):50–62. http://dx.doi.org/10.1016/0021-9045(72)90080-9.

[54] Aliabadi MH. The boundary element method, Volume 2: Applications in solids and structures. vol. 2, John Wiley & Sons; 2002.

[55] Guiggiani M, Casalini P. Direct computation of Cauchy principal value integrals in advanced boundary elements. Internat J Numer Methods Engrg 1987;24(9):1711–20. http://dx.doi.org/10.1002/nme.1620240908.

[56] Williams M. On the stress distribution at the base of a stationary crack. J Appl Mech 1957;24:109–14.

[57] Greville T. Numerical procedures for interpolation by spline functions. J Soc Ind Appl Math Series B: Numerical Analysis 1964;1(1):53–68. http://dx.doi.org/10.1137/0701005.

[58] Johnson RW. Higher order B-spline collocation at the greville abscissae. Appl Numer Math 2005;52(1):63–75. http://dx.doi.org/10.1016/j.apnum.2004.04.002.

[59] Telles J. A self-adaptive co-ordinate transformation for efficient numerical evaluation of general boundary element integrals. Internat J Numer Methods Engrg 1987;24(5):959–73. http://dx.doi.org/10.1002/nme.1620240509.

[60] Telles J, Oliveira R. Third degree polynomial transformation for boundary element integrals: further improvements. Eng Anal Bound Elem 1994;13(2):135–41. http://dx.doi.org/10.1016/0955-7997(94)90016-7.

[61] Paris PC. A rational analytic theory of fatigue. The Trend Eng 1961;13:9.

[62] Tanaka K. Fatigue crack propagation from a crack inclined to the cyclic tensile axis. Eng Fract Mech 1974;6(3):493–507. http://dx.doi.org/10.1016/0013-7944(74)90007-1.

[63] Price R, Trevelyan J. Boundary element simulation of fatigue crack growth in multi-site damage. Eng Anal Bound Elem 2014;43:67–75. http://dx.doi.org/10.1016/j.enganabound.2014.03.002.

[64] Andrade HC, Leonel ED. The multiple fatigue crack propagation modelling in nonhomogeneous structures using the DBEM. Eng Anal Bound Elem 2019;98:296–309. http://dx.doi.org/10.1016/j.enganabound.2018.10.026.

[65] Portela A, Aliabadi M, Rooke D. Dual boundary element incremental analysis of crack propagation. Comput Struct 1993;46(2):237–47. http://dx.doi.org/10.1016/0045-7949(93)90189-k.

[66] Erdogan F, Sih GC. On the crack extension in plates under plane loading and transverse shear. J Basic Eng 1963;85(4):519. http://dx.doi.org/10.1115/1.3656897.

[67] Chen FH, Shield RT. Conservation laws in elasticity of the J-integral type. Z Angew Math Phys 1977;28(1):1–22. http://dx.doi.org/10.1007/bf01590704.

[68] Fett T. Stress intensity factors - T-stresses - weight functions. Technical Report, In: Schriftenreihe des Instituts für Keramik im Maschinenbau - IKM, 50, Karlsruher Institut für Technologie (KIT); 2008, http://dx.doi.org/10.5445/KSP/1000007996.

[69] Brebbia CA, Telles JCF, Wrobel LC. Boundary element techniques: theory and applications in engineering. Springer-Verlag; 1984.

[70] Tada H, Paris PC, Irwin GR. The stress analysis of cracks handbook. 3 ed.. ASME; 2000, http://dx.doi.org/10.1115/1.801535.

[71] Liu XY, Xiao QZ, Karihaloo BL. XFEM for direct evaluation of mixed mode SIFs in homogeneous and bi-materials. Internat J Numer Methods Engrg 2004;59(8):1103–18. http://dx.doi.org/10.1002/nme.906.

[72] Judt PO, Ricoeur A. Consistent application of path-independent interaction integrals to arbitrary curved crack faces. Arch Appl Mech 2014;85(1):13–27. http://dx.doi.org/10.1007/s00419-014-0897-z.

[73] Yan X. A boundary element analysis for stress intensity factors of multiple circular arc cracks in a plane elasticity plate. Appl Math Model 2010;34(10):2722–37. http://dx.doi.org/10.1016/j.apm.2009.12.008.

[74] Choi M-J, Cho S. Isogeometric analysis of stress intensity factors for curved crack problems. Theor Appl Fract Mech 2015;75:89–103. http://dx.doi.org/10.1016/j.tafmec.2014.11.003.

[75] Pustejovsky MA. Fatigue crack propagation in titanium under general in-plane loading–I: Experiments. Eng Fract Mech 1979;11(1):9–15. http://dx.doi.org/10.1016/0013-7944(79)90025-0.

[76] Pereira JP, Duarte CA, Jiao X. Three-dimensional crack growth with hp-generalized finite element and face offsetting methods. Comput Mech 2010;46(3):431–53. http://dx.doi.org/10.1007/s00466-010-0491-3.